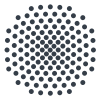

University of Stuttgart
Germany

SimTech

C. Bleiler[a,b] · **P. Ponte Castañeda**[c] · **O. Röhrle**[a,b]

A microstructurally-based, multi-scale, continuum-mechanical model of skeletal muscle tissue

Preprint

[a] Institute of Applied Mechanics (CE), University of Stuttgart,
Pfaffenwaldring 7, 70569 Stuttgart, Germany

[b] Stuttgart Centre for Simulation Sciences (SC SimTech),
Pfaffenwaldring 5a, 70569 Stuttgart, Germany

[b] Department of Mechanical Engineering and Applied Mechanics, University of Pennsylvania,
Philadelphia, PA 19104-6315, USA

Abstract This work presents a novel microstructurally-based, multi-scale model describing the passive behaviour of skeletal muscle tissue. The model is based on the detailed description of the mechanically relevant parts of the microstructure. The effective constitutive material response is obtained by a homogenisation of mechanical energies and stresses from the micro- to the macroscale. The key feature of the new model is that it does not require any constitutive assumptions or calibration on the macroscale. The effective mechanical response is a pure consequence of the stiffness and structural arrangement of microscopic components. In this sense, the model inherits its direction-dependent properties directly from the microstructure. This is achieved by employing a Voigt-type homogenisation and by utilising for the complex collageneous network of the extracellular matrix an angular integration method. For physiologically realistic microscopic model parameters, this model reveals that muscle tissue exhibits a tensile stiffness that is larger transverse to the muscle fibre than in muscle fibre direction. This highlights that muscle tissue in general does not obey a classical fibre-reinforcement solely for tensile stretches of the muscle fibres but rather a general transversely isotropic behaviour. Moreover, the formulation of the effective macroscopic energy is provided in terms of well-known macroscopic strain invariants, which allows for an easy application of the model in standard numerical settings.

Keywords Skeletal muscle · microstructure · homogenisation · collagen fibres · orientation density function

Stuttgart Research Centre for Simulation Sciences (SC SimTech)
SimTech – Cluster of Excellence
Pfaffenwaldring 5a
70569 Stuttgart
www.simtech.uni-stuttgart.de

1 Introduction

Capturing the inter- and intra-tissue variability of biological tissue within a continuum-mechanical modelling framework is a challenging and mainly unresolved task. For skeletal muscle tissue, like for many other biological tissues, this is mainly due to the fact that the overall macroscopic behaviour of the tissue is strongly influenced by various scale-dependent structural and biophysical phenomena. On a microscopic level, for example, excitable cells, the so-called sarcomeres, are responsible for the active behaviour of the skeletal muscles. Sarcomeres are the smallest functional unit within a muscle (fibre), yet they are responsible for the overall muscular force generation and, therefore, for motion. Without the complex and hierarchical network of connective tissue within the skeletal muscle, the generated forces would, however, not be transferred to the skeleton and motion would not be possible. The different collageneous layers within a skeletal muscle tissue, i. e., the endomysium, the perimysium, and the epimysium, are not only responsible for transferring the generated forces from the sarcomere to the skeleton, but also for its mechanical stability and its stiffness, i. e., its passive mechanical behaviour, see, for example MacIntosh et al. [2006] or Lieber [2010]. The collageneous structures themselves are hierarchical compounds of different collagen fibres types, e. g., of type I, III, IV, V, VI, VIII, XII, XIII, XIV, XV, XVIII, and XIX (Kovanen [2002]). The collagen type with the strongest overall influence on the mechanical material behaviour is of course tissue dependent. However, the most dominant one is typically collagen of type I. It exhibits among the different collagen types the largest contribution to the stiffness of biological tissues [Gelse et al., 2003].

Instead of exploiting this hierarchical structure and capturing its complexity, the most common constitutive models describing the overall passive mechanical behaviour of biological tissue on the organ scale appeal to phenomenological approaches. For example, the passive mechanical behaviour of skeletal muscles is typically modelled on the organ scale with transversely isotropic, fibre-reinforced material models, e. g., Johansson et al. [2000], Blemker and Delp [2005], Röhrle and Pullan [2007], Böl [2010], Ehret et al. [2011], Heidlauf and Röhrle [2013], or Sharifimajd and Stålhand [2013]. While these models are easy and efficient to implement within most computational frameworks, they are often a strong oversimplification of the actual underlying mechanical properties. For example, experiments by Böl et al. [2014] clearly showed that muscle tissue must not be described as a classical fibre-reinforced material, in which the fibre reinforcement is in muscle fibre direction and in which the muscle fibres only contribute to the tensile stiffness. In reality, the microstructure of muscle tissue has a complex collagen-fibre-reinforcement, which constitutes a distinct macroscopic reinforcement effect also when the muscle fibres are compressed.

Moreover, the phenomenological approaches are only as good as the data that has been used to calibrate them. Obtaining comprehensive (ideally in-vivo) experimental data for fitting the respective material parameters is extremely difficult. For instance, there are experimental studies, which observed that muscle tissue shows its stiffest response in the muscle fibre direction [Morrow et al., 2010], transverse to the muscle fibre direction (Takaza et al. [2013] or Mohammadkhah et al. [2016] in compression), or in a 45° angle to the muscle fibre direction (Mohammadkhah et al. [2016] in tension). Further, the strong inter- and intra-subject variations in skeletal muscle tissues would require many different experimental tests to capture the tissue-inherent variations. The required detail and the needed amount of experimental data is currently not available in the literature.

From a modelling perspective, multi-scale models are a powerful way of overcoming some of these issues. The idea of multi-scale models is to utilise suitable homogenisation and upscaling techniques to directly incorporate characteristics and properties from smaller scales into the macroscopic continuum scale. Multi-scale models have been successfully formulated for a variety of biological materials, e. g., Hurschler et al. [1997] for tendons and ligaments, Buehler [2008] for collagen, Maceri et al. [2010] for collageneous tissue, Ricken et al. [2010] for the liver, Chen et al. [2011] for fibrous tissue, Bleiler et al. [2015b] for bone-cement injection processes, Ehlers and Wagner [2015] for the brain, or by Heidlauf et al. [2016] for incorporating the mechanical behaviour of the giant protein titin into the overall behaviour of skeletal muscle tissue. More recently, skeletal-muscle-specific homogenisation techniques were proposed by Bleiler et al. [2015a, 2016] and Spyrou et al. [2017, 2019]. Those works follow the basic idea of splitting the muscle into a two-phase material consisting of muscle fibres and collageneous tissue. This is essentially similar to what Fung proposed in Chapter 9 of his seminal biomechanics book [Fung, 2010]. In (purely) micromechanical studies, this separation was also applied by Virgilio et al.

[2015]. A similar approach was followed in the structural model of Gindre et al. [2013], which, however, is not consistently formulated within the framework of continuum mechanics.

Differentiating between muscle fibre and collageneous tissue has the advantage that the mechanical (or other) properties of the two phases can be described individually without entailing the drawback of including macroscopic (fitting) parameters that smear the characteristics over the entire material. Another advantage is that there often exist more comprehensive and higher quality experimental data for microscopic constituents. Since the extracellular matrix is mainly responsible for the macroscopic mechanical characteristics and variations of skeletal muscle tissue and, hence, for a better understanding of the healthy and diseased tissue, there exists, for example, extensive work on the characterisation of collageneous extracellular matrix tissue.

In summary, purely macroscopic modelling approaches cannot be used to describe the macroscopic behaviour subject to microstructural variations in a natural way, i. e., without parameter fitting. Multi-scale models allow for a direct incorporation of microstructural variations and they provide a framework in which the influence of microstructural variations on the macroscopic behaviour can be investigated in a systematic way. Thus, we propose a novel two-phase, multi-scale model for skeletal muscle tissue that is based on a rigorous split between the two microstructural components: (i) the muscle fibre and (ii) the extracellular matrix. This approach allows to comprehensively describe each of the components and their mechanical properties and derive from that the overall mechanical behaviour of skeletal muscle tissue. The modelling approach results in analytical expressions for the effective macroscopic quantities, like the strain energy and the stresses. With this new model at hand, relevant aspects of the theory of transverse isotropy are investigated and the influence of changes within the microstructural constituents on the overall mechanical behaviour of skeletal muscle tissue will be investigated.

2 A two-phase model for skeletal muscle tissue

Inside the highly heterogeneous microstructure of skeletal muscle tissue, two structural components are mainly responsible for the mechanical characteristics of the overall material behaviour: (i) the muscle fibre, which contains the sarcomeres (the activatable units) and proteins, e. g., titin, and (ii) the extracellular matrix (ECM), which contains the collageneous tissues with various types of collagen fibres and other proteins, e. g., elastin. The muscle fibres are responsible for the excitable (active) behaviour of the muscles, while the passive stiffness is mainly due to the extracellular matrix and the collagen fibres therein. Within this work, we assume that both phases exhibit hyperelastic material behaviour. Further, we entirely focus on the passive mechanical behaviour of skeletal muscle tissue and neglect any active forces stemming from contractions within sarcomeres. In addition, we assume for both phases material incompressibility and follow an affinity assumption for the microscopic deformation fields. This is motivated by the idea that the relative motion between the components is negligible due to the strong integration of the components [Fung, 2010].

Thus, we propose a two-phase model for skeletal muscle tissue consisting of a muscle fibre phase[1] φ^{F} and an extracellular matrix phase φ^{M}. The overall muscle material φ is considered as the homogenisation of the two phases, i. e.,

$$\varphi = \bigcup_{\alpha} \varphi^{\alpha} = \varphi^{\mathrm{F}} \cup \varphi^{\mathrm{M}}, \tag{1}$$

with $\alpha \in \{\mathrm{F}, \mathrm{M}\}$. Consequently, this model constitutes a multi-scale approach, where the two phases φ^{α} live on the microscale and the overall muscle φ lives on the macroscale. The phases are homogenised at the macroscopic material point $\bar{\mathcal{P}}$ by introducing a representative volume element (RVE), see Figure 1. Thus, the effective behaviour on the macroscopic continuum scale is derived by means of homogenisation. In this field, analytical approaches were presented by, e. g., Talbot and Willis [1985], Ponte Castañeda [1991], or Nemat-Nasser and Hori [1999] and numerical approaches were proposed by, e. g., Miehe [2002], Geers et al. [2010], or Schröder [2014]. In this work, we will follow an affinity assumption and will apply an analytical Voigt-type homogenisation (see, e. g., Voigt [1887] or Hill [1963]), which was also used in the models of Gindre et al. [2013] and Spyrou et al. [2017].

[1] Note that in the context of this work, the terms *phase*, *constituent* and *component* can be used interchangeably.

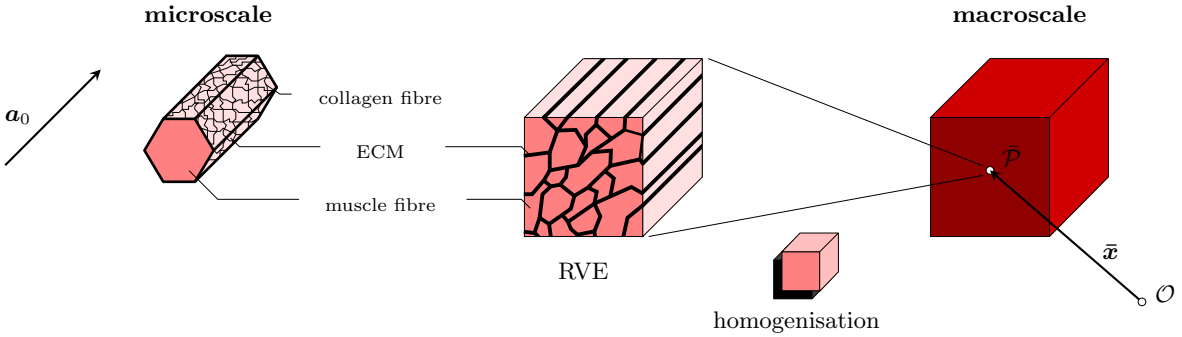

Fig. 1 Multi-scale scheme for the microstructurally-based modelling of skeletal muscle tissue.

2.1 Continuum mechanics fundamentals for materials with microstructure

Let the macroscopic body $\bar{\mathcal{B}}$ be a coherent manifold of infinite material points $\bar{\mathcal{P}} \in \bar{\mathcal{B}}$, each of them being parametrised by a position vector $\bar{\boldsymbol{X}}$ in a stress-free reference configuration. The motion of the material points to a position $\bar{\boldsymbol{x}} = \bar{\boldsymbol{\chi}}(\bar{\boldsymbol{X}})$ in an actual configuration is described by the map $\bar{\boldsymbol{\chi}}$ with deformation gradient $\bar{\boldsymbol{F}}(\bar{\boldsymbol{X}}) = \partial_{\bar{\boldsymbol{X}}}\, \bar{\boldsymbol{\chi}}(\bar{\boldsymbol{X}})$. Note, throughout this work, $\partial_\alpha\,(\cdot)$ will be used as a shorthand notation for the derivative $\frac{\partial(\cdot)}{\partial \alpha}$.

A microscopically heterogeneous material additionally has a microstructure $\mathcal{B}$ with material points $\mathcal{P} \in \mathcal{B}$ attached at every macroscopic material point $\bar{\mathcal{P}} \in \bar{\mathcal{B}}$. In direct analogy to the macroscopic considerations, the microscopic material points are defined by their referential position vector $\boldsymbol{X}$ and transported to an actual position $\boldsymbol{x} = \boldsymbol{\chi}(\boldsymbol{X})$ by the map $\boldsymbol{\chi}$. Material volume changes are described by the Jacobian $J(\boldsymbol{X}) = \det[\boldsymbol{F}(\boldsymbol{X})] > 0$, which is the determinant of the microscopic deformation gradient $\boldsymbol{F}(\boldsymbol{X}) = \partial_{\boldsymbol{X}}\, \boldsymbol{\chi}(\boldsymbol{X})$. The incompressibility assumption entails the preservation of volume and requires $J(\boldsymbol{X}) = 1$ to be satisfied at the (microscopic) material point $\mathcal{P}$.

Based on the assumption that the two phases exhibit hyperelastic material behaviour and that only passive effects are considered, the constitutive behaviour of the two phases is fully described by volume-specific, frame-indifferent strain-energy functions

$$\mathscr{W}^\alpha(\boldsymbol{Q}\boldsymbol{F}) \;=\; \mathscr{W}^\alpha(\boldsymbol{F}), \quad \forall \boldsymbol{Q} \in \mathcal{SO}(3)\,. \tag{2}$$

The local energy in the microstructure is then given by

$$\mathscr{W}(\boldsymbol{X}, \boldsymbol{F}) \;=\; \sum_\alpha \mathscr{X}^\alpha(\boldsymbol{X})\, \mathscr{W}^\alpha(\boldsymbol{F})\,, \tag{3}$$

where $\mathscr{X}^\alpha(\boldsymbol{X})$ are the characteristic functions defined by

$$\mathscr{X}^\alpha(\boldsymbol{X}) \;=\; \begin{cases} 1 & \text{if } \boldsymbol{X} \in \varphi^\alpha\,, \\ 0 & \text{else,} \end{cases} \tag{4}$$

and hence contain information about the spatial composition of the microstructure. Structural discontinuities of the microstructure are prevented by the saturation condition $\sum_\alpha \mathscr{X}^\alpha = 1$ and the jump condition $[\![\boldsymbol{u}]\!] = \boldsymbol{0}$ for the displacement vector $\boldsymbol{u} = \boldsymbol{x} - \boldsymbol{X}$. This means that the two phases are perfectly bonded at their interface. For completeness, we want to remark that the local constitutive relation for the first Piola-Kirchhoff stress is given by the so-called Doyle-Ericksen formula

$$\boldsymbol{P}(\boldsymbol{X}, \boldsymbol{F}) \;=\; \partial_{\boldsymbol{F}}\, \mathscr{W}(\boldsymbol{X}, \boldsymbol{F})\,. \tag{5}$$

2.2 Scale transition and effective quantities

So far, the mechanical problem has been fully specified on the microscale. The quantities still need to be upscaled to a macroscopic perspective. Therefore, we assume that the microstructure $\mathcal{B}$ constitutes

a representative volume element (RVE) and introduce the operation

$$\langle(\cdot)\rangle \;=\; \frac{1}{V}\int_{\mathcal{B}_0}(\cdot)\,\mathrm{d}V \;=:\; \bar{(\cdot)}\,, \tag{6}$$

which defines the averaging of a quantity $(\cdot)$ over volume $V = \mathrm{vol}[\mathcal{B}_0]$ of the referential microstructure (hence, the RVE) $\mathcal{B}_0$, see, e. g., Hill [1972]. Thus, $\bar{\boldsymbol{F}} = \langle \boldsymbol{F}\rangle$ defines the relationship between the macro- and microscopic deformation and we can formulate the effective macroscopic energy

$$\bar{\mathscr{W}} \;=\; \langle \mathscr{W}(\boldsymbol{X},\boldsymbol{F})\rangle \;=\; \sum_{\alpha} n^{\alpha}\langle \mathscr{W}^{\alpha}(\boldsymbol{F})\rangle^{\alpha}\,, \tag{7}$$

where $\langle(\cdot)\rangle^{\alpha}$ denotes the averaging of a quantity $(\cdot)$ over the volume of φ^{α} and $n^{\alpha} = \langle \mathscr{X}^{\alpha}\rangle$ describes the volume fractions of the phases. Further, the microscopic deformation is obtained through the minimum potential energy principle, i. e.,

$$\boldsymbol{F} \;=\; \arg\min_{\boldsymbol{F}\in\mathcal{K}(\bar{\boldsymbol{F}})}\langle \mathscr{W}(\boldsymbol{X},\boldsymbol{F})\rangle\,. \tag{8}$$

Therein, $\mathcal{K}(\bar{\boldsymbol{F}})$ is a set of kinematically admissible deformations fulfilling the constraint $\boldsymbol{x} = \bar{\boldsymbol{F}}\boldsymbol{X}$ on the boundary $\partial\mathcal{B}_0$ of the microstructure. Hence, combining Eqs (7) and (8) results in an expression for the effective energy $\bar{\mathscr{W}}$, which is driven by the deformation $\bar{\boldsymbol{F}}$ at the macroscopic material point $\bar{\mathcal{P}}$. For completeness, the macroscopic constitutive relation for the effective first Piola-Kirchhoff stress $\bar{\boldsymbol{P}} = \langle \boldsymbol{P}\rangle$ is given by

$$\bar{\boldsymbol{P}}(\bar{\boldsymbol{F}}) \;=\; \partial_{\bar{\boldsymbol{F}}}\,\bar{\mathscr{W}}(\bar{\boldsymbol{F}})\,, \tag{9}$$

see, e. g., Hill [1972].

Note, all macroscopic heterogeneities are characterised by an additional $\bar{\boldsymbol{X}}$-dependence of the deformation and stress measures. For the sake of readability, this notation was not explicitly enforced. Moreover, further details on the foundations of mechanics for heterogeneous materials are found in, for example, Ponte Castañeda and Suquet [1998], Nemat-Nasser and Hori [1999], or Zohdi and Wriggers [2008].

2.3 Affine microscopic deformation model

The above introduced general framework leads to non-affine deformations in the microstructure. For the specific case of skeletal muscle tissue, Fung [2010] provides arguments motivated through its underlying physiology why the relative motion of the two phases is of minor importance. Fung [2010] states that protein structures like dystrophin causes the muscle fibres and the extracellular matrix to form a very dense and closely connected unit. Further, the extracellular matrix in skeletal muscle consists of very thin layers surrounding the muscle fibres and muscle fibre bundles and most likely move with these structures. Based on these arguments, the alternative affine prescription,

$$\boldsymbol{F} \;=\; \bar{\boldsymbol{F}}\,, \tag{10}$$

for the microscopic deformation is used. From a mechanical point of view, this constitutes a Voigt-type homogenisation, see, e. g., Voigt [1887] or Hill [1963]. Beyond its simplicity, this approach has the convenient feature of being an exact homogensation for specific classes of materials under certain loading conditions.

Further, making use of definition (10) in Eq. (7) yields the effective energy $\bar{\mathscr{W}}(\bar{\boldsymbol{F}})$ as a weighted mean of the two phase energies:

$$\bar{\mathscr{W}}(\bar{\boldsymbol{F}}) \;=\; n^{\mathrm{F}}\,\mathscr{W}^{\mathrm{F}}(\bar{\boldsymbol{F}}) \;+\; n^{\mathrm{M}}\,\mathscr{W}^{\mathrm{M}}(\bar{\boldsymbol{F}}). \tag{11}$$

Assuming that both phases φ^{α} are incompressible leads for the overall muscle tissue φ to the well-known incompressibility constraint

$$\det[\bar{\boldsymbol{F}}] \;=\; \bar{J} \;=\; 1. \tag{12}$$

Splitting the overall deformation gradient into a purely volumetric part $\bar{J}^{1/3}\boldsymbol{I}$ (with $\boldsymbol{I}$ being the second-order identity) and a unimodular part $\breve{\boldsymbol{F}}$, see, e. g., Flory [1961] or Miehe [1994], one obtains

$$\bar{\boldsymbol{F}} \,=\, (\bar{J}^{1/3}\boldsymbol{I})\,\breve{\boldsymbol{F}}. \tag{13}$$

To avoid confusion, we want to remark that the unimodular/deviatoric part is usually marked by an overbar. However, this notation clashes herein with the overbar used in multi-scale studies for quantities on the macroscale. Hence, we denote the unimodular part with a breve. Further, by using $\breve{\boldsymbol{F}}$ instead of $\breve{\bar{\boldsymbol{F}}}$, we can avoid bulky notation with an acceptable sacrifice of consistency in the notation. This also implies that the energies, $\mathscr{W}^{\mathrm{F}}$ and $\mathscr{W}^{\mathrm{M}}$, of the incompressible phases, cf. Eq. (11), are evaluated at $\breve{\boldsymbol{F}}$.

Using the constitutive relation (9), one obtains the macroscopic stress that is given by

$$\bar{\boldsymbol{P}}(\bar{\boldsymbol{F}}) \,=\, n^{\mathrm{F}}\,\boldsymbol{P}^{\mathrm{F}}(\bar{\boldsymbol{F}}) \,+\, n^{\mathrm{M}}\,\boldsymbol{P}^{\mathrm{M}}(\bar{\boldsymbol{F}}) \,-\, p\,\bar{J}\,\bar{\boldsymbol{F}}^{T-1}\,, \tag{14}$$

where $\boldsymbol{P}^{\alpha} \,=\, \partial_{\bar{\boldsymbol{F}}}\,\mathscr{W}^{\alpha}$ refers to the the partial stresses and the Lagrange multiplier p ensures the incompressibility constraint. Clearly, the determinant $\bar{J} \,=\, 1$ does not contribute to the stress $\bar{\boldsymbol{P}}$, however, it remains in (14) and subsequent stress formulations to be consistent in the derivation of the fourth-order tangent modulus $\bar{\mathbb{L}} = \partial_{\bar{\boldsymbol{F}}}\bar{\boldsymbol{P}}$. Note, choosing a fully incompressible framework makes the use of a volumetric energy contribution $U(\bar{J})$ superfluous.

3 Constitutive modelling of the phases

One of the key advantages of the presented two-phase framework is that the mechanical behaviour of the two phases can be mechanically described separately, which makes the assumptions of a smeared overall material, as is is the case for phenomenological approaches, unnecessary. In the following, we introduce the constitutive material descriptions for the two phases, first for the muscle fibre phase and then for the extracellular matrix phase. As the extracellular matrix is the key contributor to the passive mechanical material behaviour, we introduce a concise model of the collagen fibres based on the angular integration model, cf., e. g., Lanir [1983], also referred to as full network model [Treloar and Riding, 1979] or microsphere model [Miehe et al., 2004], which has been successfully applied for other biological tissues [Alastrué et al., 2009, Ateshian et al., 2009, Federico and Herzog, 2008], but not yet to skeletal muscle tissue.

3.1 The muscle fibre phase φ^{F}

The muscle fibres (also known as muscle cells or, in the case of cardiac cells, myocytes) are composed of bundles of parallel myofibrils, which in turn contain the serially arranged sarcomeres. The sarcomeres are responsible for the active behaviour of muscle tissue through activation-triggered structural changes of the proteins actin and myosin. The passive stiffness of the muscle fibres is mainly addressed to another protein inside the sarcomeres called titin, see, for example, Linke et al. [1998] or Li et al. [2016] for experimental studies or Heidlauf et al. [2016, 2017] for modelling studies. Experimental studies on isolated muscle fibres by Meyer and Lieber [2011] as well as Smith et al. [2011] exhibited nearly-linear stress-strain behaviour under non-active conditions. Hence, the passive mechanical behaviour of muscle fibres is modelled using the isotropic Neo-Hookean energy formulation

$$\mathscr{W}^{\mathrm{F}} \,=\, \frac{\mu^{\mathrm{F}}}{2}\,(\breve{\boldsymbol{F}}\cdot\breve{\boldsymbol{F}} \,-\, 3), \tag{15}$$

where μ^{F} is the ground-state shear modulus of the fibre. The first Piola-Kirchoff stress of the Neo-Hookean fibre energy is then given by

$$\boldsymbol{P}^{\mathrm{F}} \,=\, \mu^{\mathrm{F}}\,\bar{J}^{-2/3}\,\mathbb{P}\,\bar{\boldsymbol{F}}\,, \tag{16}$$

where the fourth-order projection tensor

$$\mathbb{P} = \mathbb{I} - (\bar{\boldsymbol{F}}^{T-1}\otimes\bar{\boldsymbol{F}})/3 \tag{17}$$

is defined such that $\partial_{\bar{\boldsymbol{F}}}\breve{\boldsymbol{F}} = \bar{J}^{-1/3}\,\mathbb{P}^{T}$ and $\mathbb{I} = (\boldsymbol{I}\otimes\boldsymbol{I})^{\overset{23}{T}}$ is the fourth-order identity map.

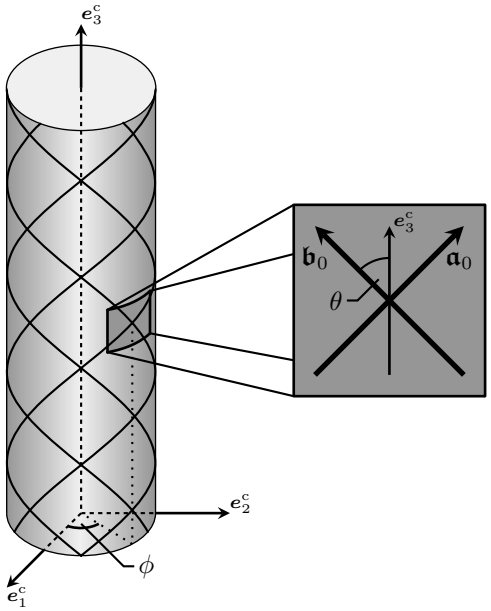

Fig. 2 Idealised muscle fibre with helically wrapped collagen fibres and the respective (tangential) unit vectors $\mathfrak{a}_0$ and $\mathfrak{b}_0$ on an infinitesimal surface element. Angle θ defines the angle between the fibre unit vectors and the coordinate vector $\mathbf{e}_3^c$.

3.2 The extracellular matrix phase φ^{M}

The mix of various types of collagen fibres as well as elastin fibres within a groundmatrix of proteoglycans is characteristic for soft biological tissues. In skeletal muscle tissue, these collageneous structures are formed by endo-, peri- and epimysium. The three different layers vary in their individual composition, especially with respect to the content of collagen type I fibres [e. g., Light and Champion, 1984]. Herein, we focus on the endo- and perimysial layers within the extracellular matrix and ignore the epimysium, since the epimysium covers the entire muscle and is therefore considered a macroscopic heterogeneity.

As proposed by Holzapfel and Weizsäcker [1998], we additively split the strain energy of the extracellular matrix into an isotropic groundmatrix part $\mathscr{W}_{\mathrm{g}}^{\mathrm{M}}$ and a generally anisotropic part $\mathscr{W}_{\mathrm{c}}^{\mathrm{M}}$ describing the collagen reinforcement, i. e.,

$$\mathscr{W}^{\mathrm{M}} = \mathscr{W}_{\mathrm{g}}^{\mathrm{M}} + \mathscr{W}_{\mathrm{c}}^{\mathrm{M}} . \tag{18}$$

The isotropic contribution is described by the Neo-Hookean energy

$$\mathscr{W}^{\mathrm{M}} = \frac{\mu^{\mathrm{M}}}{2} \left(\breve{\boldsymbol{F}} \cdot \breve{\boldsymbol{F}} - 3 \right) , \tag{19}$$

where μ^{M} is the ground-state shear modulus of the groundmatrix. The first Piola-Kirchhoff stress is derived from $\mathscr{W}^{\mathrm{M}}$ and is given by

$$\boldsymbol{P}^{\mathrm{M}} = \mu^{\mathrm{M}} \, \bar{J}^{-2/3} \, \mathbb{P} \, \bar{\boldsymbol{F}} . \tag{20}$$

As for a variety of biological tissues, the collagen reinforcement within skeletal muscles is characterised by the helical arrangement of collagen fibres. This is true for each of the different layers of the extracellular matrix [e. g., Purslow, 2010, Purslow and Trotter, 1994]. The collagen fibres usually obey directions of preferred alignments and a dispersion around those mean directions. Thus, the starting point for modelling the helical collagen reinforcement is a geometrical model of an idealised muscle fibre/muscle fibre bundle (cf. Figure 2). To rigorously follow the ideas of homogenisation, the polygonal anatomy of a muscle fibre, as, for example, illustrated by the RVE in Figure 1, is approximated by a circle. In an averaged sense, a circle is assumed to best describe the shape heterogeneities. A similar argument holds for approximating the irregular geometrical shape of muscle fibre bundles.

Assuming such idealised geometries for muscle fibres/muscle fibre bundles, a surface element contains two (mechanically equivalent) fibre families (clock- and counter-clockwise), which are parametrised by the two unit vectors

$$\begin{aligned} \mathfrak{a}_0(\theta,\phi) &= -\sin[\theta]\sin[\phi]\boldsymbol{e}_1^c + \sin[\theta]\cos[\phi]\boldsymbol{e}_2^c + \cos[\theta]\boldsymbol{e}_3^c, \\ \mathfrak{b}_0(\theta,\phi) &= +\sin[\theta]\sin[\phi]\boldsymbol{e}_1^c - \sin[\theta]\cos[\phi]\boldsymbol{e}_2^c + \cos[\theta]\boldsymbol{e}_3^c \end{aligned} \tag{21}$$

and thus fully specified through a polar angle $\theta \in [0,\pi]$ and an azimuthal angle $\phi \in [0,2\pi)$. Further, the Cartesian coordinate system $\boldsymbol{e}_i^s$ $(i=1,2,3)$ is aligned such that the direction $\boldsymbol{e}_3^s$ is collinear with the muscle fibre direction, which will be denoted by $\boldsymbol{a}_0$, see Figure 1. To account for the statistical orientation and dispersion of the collagen fibres, we assume the existence of an orientation density function (ODF) as introduced by, e. g., Lanir [1983]:

$$\mathfrak{p}^\zeta(\mathfrak{a}_0) \;=\; \mathfrak{p}^\zeta(\mathfrak{b}_0) \;=\; \mathfrak{p}_\theta^\zeta(\theta)\,\mathfrak{p}_\phi^\zeta(\phi)\,. \tag{22}$$

Therein, we implied that both fibre families have the same ODF and that the function can be split into a polar part $\mathfrak{p}_\theta^\zeta(\theta)$ and an azimuthal part $\mathfrak{p}_\phi^\zeta(\phi)$.

The extracellular matrix of biological tissue may contain several distinct collagen fibre types with individual orientations and fibre dispersions. To account for this flexibility, an ODF is introduced for each fibre type and denoted with a superscript ζ.

The structure of the fibre unit vectors, $\mathfrak{a}_0$ and $\mathfrak{b}_0$, together with the range of the angles θ and ϕ exhibits similarities with classical spherical coordinates. Thus, each of the vectors $\mathfrak{a}_0$ or $\mathfrak{b}_0$ points with probability $\mathfrak{p}^\zeta$ to an infinitesimal area element $\mathrm{d}\Omega = \sin[\theta]\,\mathrm{d}\theta\,\mathrm{d}\phi$ of the unit sphere surface Ω. By assuming normalised probability functions $\mathfrak{p}^\zeta$, we obtain

$$\begin{aligned} &\int_\Omega \mathfrak{p}_\theta^\zeta(\theta)\,\mathfrak{p}_\phi^\zeta(\phi)\,\mathrm{d}\Omega \\ &\qquad = \int_0^{2\pi}\int_0^{\pi} \mathfrak{p}_\theta^\zeta(\theta)\,\mathfrak{p}_\phi^\zeta(\phi)\,\sin[\theta]\,\mathrm{d}\theta\,\mathrm{d}\phi \;=\; 1\,. \end{aligned} \tag{23}$$

Further, we assume for the azimuthal distribution a homogeneous relation, i. e., $\mathfrak{p}_\phi^\zeta = \mathfrak{p}_\phi = 1/(2\pi)$. For the polar ODF, we make use of the π-periodic von-Mises-function

$$\tilde{\mathfrak{p}}_\theta^\zeta(\theta) \;=\; \frac{\exp\left[b^\zeta\,\cos[2\,(\theta\,-\,\theta_{\mathrm{m}}^\zeta)]\right]}{2\,\pi\,I_0(b^\zeta)}\,, \tag{24}$$

where $\theta_{\mathrm{m}}^\zeta$ is the mean of the distribution of a specific collagen fibre type, b^ζ is a parameter for the spreading around the mean, and $I_0(b^\zeta) = 1/\pi\int_0^\pi \exp\left[b^\zeta\,\cos[\theta]\right]\mathrm{d}\theta$ is the modified Bessel function of first kind of order zero. After a consistent normalisation due to Eq. (23), the resulting polar ODF is given by $\mathfrak{p}_\theta^\zeta(\theta) = \tilde{\mathfrak{p}}_\theta^\zeta(\theta)/I^\zeta$, where $I^\zeta = \int_0^\pi \tilde{\mathfrak{p}}_\theta^\zeta(\theta)\,\sin[\theta]\,\mathrm{d}\theta$.

The kinematics of the two fibre families are defined by the maps

$$\mathfrak{a}(\theta,\phi) \;=\; \mathfrak{F}_{\mathfrak{a}}^\zeta\,\mathfrak{a}_0(\theta,\phi) \quad\text{and}\quad \mathfrak{b}(\theta,\phi) \;=\; \mathfrak{F}_{\mathfrak{b}}^\zeta\,\mathfrak{b}_0(\theta,\phi)\,, \tag{25}$$

which transport the referential vectors $\mathfrak{a}_0$ and $\mathfrak{b}_0$ to the vectors $\mathfrak{a}$ and $\mathfrak{b}$ within the actual configuration, respectively. The latter vectors contain the information about the reorientation as well as the actual stretches, $\lambda_{\mathfrak{a}}$ and $\lambda_{\mathfrak{b}}$, which are calculated by

$$\begin{aligned} \lambda_{\mathfrak{a}}(\theta,\phi) &= \sqrt{\mathfrak{a}(\theta,\phi)\cdot\mathfrak{a}(\theta,\phi)} \quad\text{and} \\ \lambda_{\mathfrak{b}}(\theta,\phi) &= \sqrt{\mathfrak{b}(\theta,\phi)\cdot\mathfrak{b}(\theta,\phi)}\,. \end{aligned} \tag{26}$$

While the distinct second-order tensors $\mathfrak{F}_{\mathfrak{a}}^\zeta$ and $\mathfrak{F}_{\mathfrak{b}}^\zeta$ defined in Eq. (25) allow for individual (non-affine) deformations, we assume in this work affine deformations within the extracellular matrix. Hence, the mapping tensors $\mathfrak{F}_{\mathfrak{a}}^\zeta$ and $\mathfrak{F}_{\mathfrak{b}}^\zeta$ coincide with the macroscopic deformation gradient, i. e.,

$$\mathfrak{F}_{\mathfrak{a}}^\zeta \;=\; \mathfrak{F}_{\mathfrak{b}}^\zeta \;=\; \bar{\boldsymbol{F}}\,. \tag{27}$$

Note, using in Eq. (27) the deviatoric part $\breve{\boldsymbol{F}}$ instead of $\bar{\boldsymbol{F}}$ may lead to undesired results even for the incompressible case [cf., Helfenstein et al., 2010, Sansour, 2008].

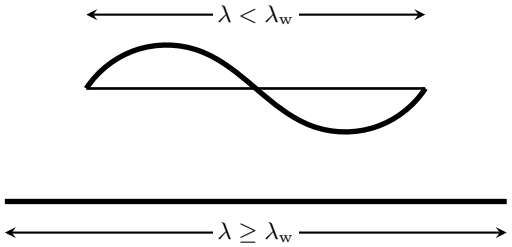

Fig. 3 Curled and uncurled state of a collagen fibre. Stretches are defined by the end-to-end length.

Before introducing an energy formulation for a single fibre, we want to remark that collagen fibres in the unloaded state are usually crimped and get uncurled under tensile loads. The stretch at which a fibre becomes completely uncurled is denoted by $\lambda_{\mathrm{w}}^{\zeta}$. In this sense, $\lambda_{\mathrm{w}}^{\zeta}$ represents a parameter for the waviness of a fibre. Thus, the vector describing a single fibre and the respective stretch are always defined based on the end-to-end length rather than on the contour length, as illustrated in Figure 3. Fully in line with the well-known assumption that a fibre only stores energy when it is subjected to tensile stretches in the uncurled state, the strain energy for a single fibre is given by

$$\mathscr{W}_{\mathrm{cf}}^{\zeta}(\lambda) = \begin{cases} \dfrac{\mu_{\mathrm{cf}}^{\zeta}}{2}\,(\lambda - \lambda_{\mathrm{w}}^{\zeta})^2 & \text{if } \lambda > \lambda_{\mathrm{w}}^{\zeta} \\ 0 & \text{else}\,, \end{cases} \tag{28}$$

where $\mu_{\mathrm{cf}}^{\zeta}$ denotes the individual collagen stiffness parameters, $\lambda_{\mathrm{w}}^{\zeta}$ are the waviness parameters, and $\mathscr{W}_{\mathrm{cf}}^{\zeta}$ are the energies for the respective collagen fibre types ζ. The fibre energy in (28), reminiscent to the energy of a linear spring, is also used by, e. g., Lanir [1979] or Decraemer et al. [1980].

To obtain the overall strain energy of the collageneous network, we define the weighted continuous average

$$\big\langle (\cdot) \big\rangle_{\Omega}^{\zeta} = \int_{\Omega} \mathfrak{p}_{\theta}^{\zeta}(\theta)\, \mathfrak{p}_{\phi}\, (\cdot)\, \mathrm{d}\Omega \tag{29}$$

of a quantity $(\cdot)$ over the surface of the unit sphere. Subsequently, the average $\langle \mathscr{W}_{\mathrm{cf}}^{\zeta} \rangle_{\Omega}^{\zeta}$ depicts the network energy of the collagen fibre type ζ, see, e. g., Lanir [1979], Miehe et al. [2004], or Alastrué et al. [2009]. Note that the normalisation condition (23) entails

$$\langle 1 \rangle_{\Omega}^{\zeta} = 1. \tag{30}$$

By exploiting the periodicity of the vectors $\mathfrak{a}_0$ and $\mathfrak{b}_0$, it becomes clear that any differences of the two fibre families will be averaged out. They will equally contribute to the averaged quantities. Hence, in the subsequent formulations for the energy and the stress, it suffices to account for the contribution of one fibre family twice. Further, the contribution of each collagen fibre type will be taken into consideration by introducing volume fractions n^{ζ} for the individual collagen fibre types with the saturation condition $\sum_{\zeta} n^{\zeta} = 1$. Consequently, the resulting energy $\mathscr{W}_{\mathrm{c}}^{\mathrm{M}}$ for the collageneous part of the extracellular matrix phase is obtained by the sum over the different collagen fibre types, i. e.,

$$\mathscr{W}_{\mathrm{c}}^{\mathrm{M}} = 2 \sum_{\zeta} n^{\zeta} \left\langle \mathscr{W}_{\mathrm{cf}}^{\zeta}(\lambda_{\mathfrak{a}}) \right\rangle_{\Omega}^{\zeta}. \tag{31}$$

The predominant collagen fibres in the extracellular matrix of skeletal muscles are the collagen of type I and III. Both collagen types add up to a volume fraction of about 95% of the total collagen amount in the endomysium, see, e. g., Duance et al. [1977], Light and Champion [1984], and Listrat et al. [1999]. As it is known that especially collagen of type I plays an important role for the mechanical behaviour of biological tissues [Gelse et al., 2003], we restrict ourselves to the consideration of type I fibres, resulting in $\zeta = \{\mathrm{I}\}$. This assumption is justified as collagen fibres of type III are much more compliant than fibres of type I [Asgari et al., 2017]. Moreover, collagen fibres of type III form a more loose mesh of fibres [Kovanen, 2002] and are therefore, from a structural point of view, less aligned than collagen type I fibres.

Combining all arguments and definitions from above leads for the anisotropic network energy to the following compact form

$$\mathscr{W}_{\mathrm{c}}^{\mathrm{M}} \;=\; 2\,n^{\mathrm{I}}\,\big\langle \mathscr{W}_{\mathfrak{cf}}(\lambda_{\mathfrak{a}})\big\rangle_{\Omega}, \tag{32}$$

where n^{I} is the volume fraction of type I collagen. For the sake of a compact notation, we omit from (32) onwards the superscript I for operator $\langle(\cdot)\rangle_{\Omega}^{\mathrm{I}}$, i. e.$\langle(\cdot)\rangle_{\Omega} = \langle(\cdot)\rangle_{\Omega}^{\mathrm{I}}$, as well as for $\mu_{\mathfrak{cf}}^{\mathrm{I}}$, $\lambda_{\mathrm{w}}^{\mathrm{I}}$, $\theta_{\mathrm{m}}^{\mathrm{I}}$.

By sequential application of the chain rule and defining $P_{\mathfrak{cf}}$ as the non-negative collagen fibre stress scalar, i. e.,

$$P_{\mathfrak{cf}}(\lambda) \;=\; \partial_{\lambda}\,\mathscr{W}_{\mathfrak{cf}} \;=\; \begin{cases} \mu_{\mathfrak{cf}}\,(\lambda-\lambda_{\mathrm{w}}) & \text{if } \lambda>\lambda_{\mathrm{w}} \\ 0 & \text{else}\,, \end{cases} \tag{33}$$

one obtains the first Piola-Kirchhoff stress,

$$\boldsymbol{P}_{\mathrm{c}}^{\mathrm{M}} \;=\; \partial_{\bar{\boldsymbol{F}}}\,\mathscr{W}_{\mathrm{c}}^{\mathrm{M}} \;=\; 2\,n^{\mathrm{I}}\,\Big\langle \frac{P_{\mathfrak{cf}}(\lambda_{\mathfrak{a}})}{\lambda_{\mathfrak{a}}}\,\mathfrak{a}\otimes\mathfrak{a}_0\Big\rangle_{\Omega}\,, \tag{34}$$

for the anisotropic matrix part.

Note, the tensor base $\mathfrak{a}\otimes\mathfrak{a}_0$ (or, analogically, the tensor base $\mathfrak{b}\otimes\mathfrak{b}_0$) in Eq. (34) can alternatively be expressed by means of a structure tensor $\boldsymbol{M}_{\mathfrak{a}} = \mathfrak{a}_0\otimes\mathfrak{a}_0$ as $\mathfrak{a}\otimes\mathfrak{a}_0 = \bar{\boldsymbol{F}}\boldsymbol{M}_{\mathfrak{a}}$ [cf., e. g., Boehler, 1979, Schröder and Neff, 2003]. As $\bar{\boldsymbol{F}}$ is independent of the angles θ and ϕ, it is possible to pull $\bar{\boldsymbol{F}}$ in front of the averaging operation. Note, an averaging operation $\langle\boldsymbol{M}_{\mathfrak{a}}\rangle_{\Omega}$ would lead to formulations that are in line with the orientation tensor introduced by Advani and Tucker III [1987].

4 Invariant-based formulation of the skeletal muscle model

The previously introduced Neo-Hookean constitutive relations for the muscle fibre and the ECM's groundmatrix, i. e., Eqs (15) and (19), are independent of any reference system. In contrast, the anisotropic energy contribution $\mathscr{W}_{\mathrm{c}}^{\mathrm{M}}$, as defined in (31), was formulated with respect to the $\boldsymbol{e}_i^{\mathrm{c}}$-coordinate system, cf. Figure 2. In that coordinate system, the $\boldsymbol{e}_3^{\mathrm{c}}$-direction was chosen to be collinear with the muscle fibre direction $\boldsymbol{a}_0$ while the $\boldsymbol{e}_1^{\mathrm{c}}$- and $\boldsymbol{e}_2^{\mathrm{c}}$-directions were chosen such that they are within the plane transverse to $\boldsymbol{a}_0$. Therefore, $\boldsymbol{e}_1^{\mathrm{c}}$ and $\boldsymbol{e}_2^{\mathrm{c}}$ are not unique as they can be rotated by any angle around $\boldsymbol{e}_3^{\mathrm{c}}$ without violating the assumptions. However, since the integration within the operator $\langle(\cdot)\rangle_{\Omega}$ is performed around the azimuthal angle ϕ, a rotation around $\boldsymbol{e}_3^{\mathrm{c}}$ does not influence the results of computing $\langle(\cdot)\rangle_{\Omega}$. This rotation invariance causes the overall material, φ, to exhibit transversely isotropic behaviour and a unit vector $\bar{\boldsymbol{a}}_0$ is defined as the macroscopic preferred direction. Consequently, $\bar{\boldsymbol{a}}_0$ is collinear to the muscle fibre direction $\boldsymbol{a}_0$ and to $\boldsymbol{e}_3^{\mathrm{c}}$.

At this point, it is important to highlight that the transversely isotropic behaviour of the overall muscle model is a direct consequence of the microstructural considerations and not a macroscopic constitutive assumption. For instance, the choice of an elliptical, non-circular cross section of the idealised muscle fibre in Figure 2 would entail an orthotropic overall behaviour.

Further, the transverse isotropy of the overall muscle allows to express the macroscopic energy $\bar{\mathscr{W}}$ in terms of the macroscopic left Cauchy-Green tensor $\bar{\boldsymbol{C}} = \bar{\boldsymbol{F}}^{T}\bar{\boldsymbol{F}}$ and a macroscopic structure tensor $\bar{\boldsymbol{M}} = \bar{\boldsymbol{a}}_0\otimes\bar{\boldsymbol{a}}_0$. The dependence on these two tensors can be replaced by a set $\mathcal{S}_1 = \{\bar{I}_1,\bar{I}_2,\bar{I}_3,\bar{J}_4,\bar{J}_5\}$ of scalar invariants, which serves as an integrity basis for the argument tensors $\bar{\boldsymbol{C}}$ and $\bar{\boldsymbol{M}}$, see, for example, Spencer [1971]. The scalar invariants are defined as:

$$\begin{gathered} \bar{I}_1 \;=\; \mathrm{tr}[\bar{\boldsymbol{C}}]\,,\quad \bar{I}_2 \;=\; \mathrm{tr}\big[\mathrm{cof}[\bar{\boldsymbol{C}}]\big]\,,\quad \bar{I}_3 \;=\; \bar{J}^2 \;=\; \det[\bar{\boldsymbol{C}}]\,, \\ \bar{J}_4 \;=\; \mathrm{tr}[\bar{\boldsymbol{C}}\bar{\boldsymbol{M}}]\,,\quad \text{and}\quad \bar{J}_5 \;=\; \mathrm{tr}[\bar{\boldsymbol{C}}^2\bar{\boldsymbol{M}}]\,. \end{gathered} \tag{35}$$

The scalar argument $\breve{\boldsymbol{F}}\cdot\breve{\boldsymbol{F}}$, as used in Eqs (15) and (19), is equal to the first invariant $\breve{I}_1 = \mathrm{tr}[\breve{\boldsymbol{C}}]$ of the unimodular right Cauchy-Green tensor $\breve{\boldsymbol{C}} = J^{-2/3}\bar{\boldsymbol{C}}$, thus ensuring a rigorous invariant-based formulation of the Neo-Hookean energies $\mathscr{W}^{\mathrm{F}}$ and $\mathscr{W}_{\mathrm{g}}^{\mathrm{M}}$. In addition, we introduce an invariant formulation

for $\mathscr{W}_{\mathrm{c}}^{\mathrm{M}}$. For this purpose, it proofs useful to take an alternative invariant set $\mathcal{S}_2 = \{\bar{\lambda}_{\mathrm{l}}, \bar{\lambda}_{\mathrm{t}}, \bar{\gamma}_{\mathrm{l}}, \bar{\gamma}_{\mathrm{t}}, \bar{\psi}_\gamma\}$, which can be computed from $\mathcal{S}_1$ by means of the following relations:

$$\begin{aligned}
\bar{\lambda}_{\mathrm{l}} &= \sqrt{\bar{J}_4}\,, \\
\bar{\lambda}_{\mathrm{t}} &= \sqrt[4]{\bar{I}_3/\bar{J}_4}\,, \\
\bar{\gamma}_{\mathrm{l}} &= \sqrt{\bar{J}_5/\bar{J}_4 - \bar{J}_4}\,, \\
\bar{\gamma}_{\mathrm{t}} &= \sqrt{\bar{I}_1 - \bar{J}_5/\bar{J}_4 - 2\sqrt{\bar{I}_3/\bar{J}_4}}\,, \\
\tan[2\bar{\psi}_\gamma] &= \frac{2\,\bar{\lambda}_{\mathrm{t}}\,H \mp \bar{\gamma}_{\mathrm{t}}\sqrt{\bar{\gamma}_{\mathrm{l}}^4\,\bar{\gamma}_{\mathrm{t}}^2\,(4\,\bar{\lambda}_{\mathrm{t}}^2 + \bar{\gamma}_{\mathrm{t}}^2) - H^2}}{\bar{\gamma}_{\mathrm{t}}\,H \pm 2\,\bar{\lambda}_{\mathrm{t}}\sqrt{\bar{\gamma}_{\mathrm{l}}^4\,\bar{\gamma}_{\mathrm{t}}^2\,(4\,\bar{\lambda}_{\mathrm{t}}^2 + \bar{\gamma}_{\mathrm{t}}^2) - H^2}}
\end{aligned} \tag{36}$$

with $H = (2\,\bar{\lambda}_{\mathrm{l}}^2 + \bar{\gamma}_{\mathrm{l}}^2)(2\,\bar{\lambda}_{\mathrm{t}}^2 + \bar{\gamma}_{\mathrm{t}}^2) + 2\,\bar{\lambda}_{\mathrm{t}}^4 - 2\,\bar{I}_2$, see, e. g., Ericksen and Rivlin [1954] or deBotton et al. [2006]. The advantage of $\mathcal{S}_2$ is the direct link between the invariants and their physical meaning with respect to a transversely isotropic material, namely, $\bar{\lambda}_{\mathrm{l}} > 0$ is a measure for the stretch along the preferred direction, $\bar{\lambda}_{\mathrm{t}} > 0$ is a stretch transverse to the preferred axis, $\bar{\gamma}_{\mathrm{l}} \geq 0$ is the shear along the axis (out-of-plane or along-fibre), and $\bar{\gamma}_{\mathrm{t}} \geq 0$ is the transverse (in-plane or cross-fibre) shear. Further, $\bar{\psi}_\gamma \in [0, \pi)$ is π-periodic and can be interpreted as a coupling measure between the different shear deformations. In addition, if $\bar{\gamma}_{\mathrm{l}}\,\bar{\gamma}_{\mathrm{t}} = 0$, then $\bar{\psi}_\gamma$ can be chosen arbitrarily, e. g., $\bar{\psi}_\gamma = 0$. Moreover, exploiting the incompressibility condition, $\bar{J} = 1$, results in $\bar{\lambda}_{\mathrm{t}} = \bar{\lambda}_{\mathrm{l}}^{-1/2}$. This can be used to further reduce the integrity bases for $\mathscr{W}_{\mathrm{c}}^{\mathrm{M}}$ to $\mathcal{S}_1 = \{\bar{I}_1, \bar{I}_2, \bar{J}_4, \bar{J}_5\}$ and $\mathcal{S}_2 = \{\bar{\lambda}_{\mathrm{l}}, \bar{\gamma}_{\mathrm{l}}, \bar{\gamma}_{\mathrm{t}}, \bar{\psi}_\gamma\}$. Following deBotton et al. [2006], it is now possible to express any arbitrary deformation gradient as a product of a proper orthogonal rotation and a generic deformation gradient of the form

$$\bar{\boldsymbol{F}}^{\mathrm{c}} = \begin{bmatrix} \bar{\lambda}_{\mathrm{l}}^{-1/2} & 0 & 0 \\ \bar{\gamma}_{\mathrm{t}} & \bar{\lambda}_{\mathrm{l}}^{-1/2} & 0 \\ \bar{\gamma}_{\mathrm{l}}\cos[\bar{\psi}_\gamma] & \bar{\gamma}_{\mathrm{l}}\sin[\bar{\psi}_\gamma] & \bar{\lambda}_{\mathrm{l}} \end{bmatrix} \boldsymbol{e}_i^{\mathrm{c}} \otimes \boldsymbol{e}_j^{\mathrm{c}}\,. \tag{37}$$

As indicated by the tensor base in Eq. (37), $\bar{\boldsymbol{F}}^{\mathrm{c}}$ has the convenient feature of being properly aligned with the $\boldsymbol{e}_i^{\mathrm{c}}$-coordinate system. Hence, it is straightforward to use $\bar{\boldsymbol{F}}^{\mathrm{c}}$ as a generic tensor argument for the fibre evolution in Eq. (27). This way, the stretch $\lambda_{\mathfrak{a}}$ as defined by Eq. (26) can be directly formulated in terms of the macroscopic invariants as

$$\begin{aligned}
\lambda_{\mathfrak{a}}(\bar{\lambda}_{\mathrm{l}}, \bar{\gamma}_{\mathrm{l}}, \bar{\gamma}_{\mathrm{t}}, \bar{\psi}_\gamma; \theta, \phi) = \big\{ & \bar{\lambda}_{\mathrm{l}}^{-1}\sin^2[\theta]\sin^2[\phi] + \\
& + (\bar{\lambda}_{\mathrm{l}}^{-1/2}\sin[\theta]\cos[\phi] - \bar{\gamma}_{\mathrm{t}}\sin[\theta]\sin[\phi])^2 + \\
& + (\bar{\lambda}_{\mathrm{l}}\cos[\theta] - \bar{\gamma}_{\mathrm{l}}\sin[\theta]\sin[\phi - \bar{\psi}_\gamma])^2 \big\}^{1/2}\,,
\end{aligned} \tag{38}$$

which relates the anisotropic (transversely isotropic) energy $\mathscr{W}_{\mathrm{c}}^{\mathrm{M}}$ directly to the invariant sets $\mathcal{S}_1$ and $\mathcal{S}_2$ via

$$\mathscr{W}_{\mathrm{c}}^{\mathrm{M}}(\bar{\boldsymbol{C}}, \bar{\boldsymbol{M}}) = \mathscr{W}_{\mathrm{c}}^{\mathrm{M}}(\mathcal{S}_1) = \mathscr{W}_{\mathrm{c}}^{\mathrm{M}}(\mathcal{S}_2) = \mathscr{W}_{\mathrm{c}}^{\mathrm{M}}(\bar{\boldsymbol{F}}^{\mathrm{c}})\,. \tag{39}$$

Proceeding with the set $\mathcal{S}_2$ and making repeated use of the chain rule leads to the formulation

$$\begin{aligned}
\boldsymbol{P}_{\mathrm{c}}^{\mathrm{M}} &= \partial_{\bar{\boldsymbol{F}}}\mathscr{W}_{\mathrm{c}}^{\mathrm{M}}(\mathcal{S}_2) \\
&= 2\,n^{\mathrm{I}}\,\big\langle P_{\mathfrak{cf}}(\lambda_{\mathfrak{a}}) \sum_{\mathfrak{I}\in\mathcal{S}_2} \{\partial_{\mathfrak{I}}\lambda_{\mathfrak{a}}\,\partial_{\bar{\boldsymbol{F}}}\mathfrak{I}\}\big\rangle_{\Omega}\,.
\end{aligned} \tag{40}$$

for the first Piola-Kirchhoff stress. Therein, each of the four summands consists of a scalar-valued derivative $\partial_{\mathfrak{I}}\lambda_{\mathfrak{a}}$ and a tensor base $\partial_{\bar{\boldsymbol{F}}}\mathfrak{I}$, where $\mathfrak{I} \in \mathcal{S}_2$. The explicit relations for the eight derivatives are provided in A. Note that the tensor bases are independent of the angles θ and ϕ and can be pulled out of the integrals in Eq. (40). If the invariant set $\mathcal{S}_1$ is used to describe the energy $\mathscr{W}_{\mathrm{c}}^{\mathrm{M}}$, one might need to conduct further applications of the chain rule when computing $\partial_{\mathfrak{I}}\mathcal{I}$ for $\mathcal{I} \in \mathcal{S}_1$ and $\mathfrak{I} \in \mathcal{S}_2$. This,

parameter	classification	interpretation
n^{M}	structural	volume fraction of the extracellular matrix
n^{I}	structural	volume fraction of type I collagen fibres inside the extracellular matrix
μ^{F}	material	(passive) stiffness of the muscle fibre
μ^{M}	material	stiffness of the isotropic groundmatrix of the extracellular matrix
$\mu_{\mathfrak{cf}}$	material	stiffness of type I collagen fibres/fibrils
λ_{w}	structural	waviness of the type I collagen fibres
θ_{m}	structural	mean preferred orientation of the type I collagen fibres
b	structural	spreading/dispersion of the type I collagen fibres

Table 1 Summary of the modelling parameters for the presented skeletal muscle model, their classification into material or structural parameters, and their biophysical interpretation with respect to the multi-scale modelling approach.

however, can be straightforwardly derived by expressing the quantities in $\mathcal{S}_1$ in terms of quantities of $\mathcal{S}_2$, i. e.,

$$\begin{aligned}\bar{I}_1 &= \bar{\lambda}_{\mathrm{l}}^2 + 2\,\bar{\lambda}_{\mathrm{t}}^2 + \bar{\gamma}_{\mathrm{l}}^2 + \bar{\gamma}_{\mathrm{t}}^2\,,\\ \bar{I}_2 &= \big((2\,\bar{\lambda}_{\mathrm{l}}^2 + \bar{\gamma}_{\mathrm{l}}^2)(2\,\bar{\lambda}_{\mathrm{t}}^2 + \bar{\gamma}_{\mathrm{t}}^2) + 2\,\bar{\lambda}_{\mathrm{t}}^4 -\\ &\quad - \bar{\gamma}_{\mathrm{l}}^2\,\bar{\gamma}_{\mathrm{t}}\,(2\,\bar{\lambda}_{\mathrm{t}}\,\sin[2\bar{\psi}_\gamma] + \bar{\gamma}_{\mathrm{t}}\,\cos[2\bar{\psi}_\gamma])\big)/2\,,\\ \bar{I}_3 &= \bar{\lambda}_{\mathrm{l}}^2\,\bar{\lambda}_{\mathrm{t}}^4\,,\quad \bar{J}_4 = \bar{\lambda}_{\mathrm{l}}^2\,,\quad \bar{J}_5 = \bar{\lambda}_{\mathrm{l}}^2\,(\bar{\lambda}_{\mathrm{l}}^2 + \bar{\gamma}_{\mathrm{l}}^2)\,.\end{aligned} \tag{41}$$

In conclusion, the invariant-based formulation of the anisotropic matrix energy $\mathscr{W}_{\mathrm{c}}^{\mathrm{M}}$ given in Eq. (39) together with the natural invariance of the Neo-Hookean energies $\mathscr{W}^{\mathrm{F}}$ and $\mathscr{W}_{\mathrm{g}}^{\mathrm{M}}$ results in an invariant-based, frame-indifferent, transversely isotropic formulation of the overall energy $\bar{\mathscr{W}}$:

$$\bar{\mathscr{W}}(\bar{\boldsymbol{C}}, \bar{\boldsymbol{M}}) = \bar{\mathscr{W}}(\mathcal{S}_1) = \bar{\mathscr{W}}(\mathcal{S}_2)\,. \tag{42}$$

5 Model parameters

The homogenisation principles in Section 2 in connection with the constitutive modelling of the micro-constituents in Section 3 results in an overall model for skeletal muscle tissue with eight model parameters. Table 1 summarises these parameters, classifies them as material or structural parameters, and provides a biophysical interpretation. The three material parameters μ^{F}, μ^{M}, $\mu_{\mathfrak{cf}}$ are directly connected to stiffnesses of the microstructural components, whereas the two volume fractions n^{M}, n^{I} refer to the microstructural composition of the material and the three remaining parameters λ_{w}, θ_{m}, b characterise the structure of the collagen type I fibre network. It becomes obvious that especially the collagen network plays a key role within this new modelling approach. The choice of specific model parameters is a crucial step towards a meaningful material model, thus, we aim to give a broad overview over literature data and variations of the three material and the five structural parameters in this section.

5.1 Material parameters

As shown in Table 1, the proposed model contains three material parameters related to stiffness of microstructural components. One of the parameters describes the stiffness of the muscle fibres while the other two describe stiffnesses inside the extracellular matrix structure.

5.1.1 Muscle fibre

The choice for a Neo-Hookean energy for the description of the muscle fibres was motivated in Section 3 by the nearly-linear stretch-stress relationships observed by Meyer and Lieber [2011] and Smith et al. [2011]. Consequently, the data of Smith et al. [2011] are used for the estimation of the material parameter μ^{F}. Therein, the relevant experiments are performed on isolated muscle fibres of human gracilis and semitendinosus muscles.

Taking the reported averaged sarcomere slack length of $2.31\,\mu$m [Smith et al., 2011] as the stress-free reference configuration, a standard least-squares fitting routine yields the parameter $\mu^{\mathrm{F}}_{\mathrm{grac}} =$

$12.452\,\mathrm{kN/m^2}$ for the gracilis muscle data and $\mu^{\mathrm{F}}_{\mathrm{semi}} = 14.440\,\mathrm{kN/m^2}$ for the semitendinosus muscle data. Utilising both muscle data in a single optimisation step, an averaged parameter for the muscle fibre of $\mu^{\mathrm{F}} = 13.446\,\mathrm{kN/m^2}$ is obtained. This is equivalent to the mean between $\mu^{\mathrm{F}}_{\mathrm{grac}}$ and $\mu^{\mathrm{F}}_{\mathrm{semi}}$. Recalling that the muscle fibre stiffness is of less influence on the overall muscle stiffness and the fact that $\mu^{\mathrm{F}}_{\mathrm{grac}}$ and $\mu^{\mathrm{F}}_{\mathrm{semi}}$ differ only moderately, we proceed with $\mu^{\mathrm{F}} = 13.446\,\mathrm{kN/m^2}$ to describe the mechanical behaviour of the skeletal muscle fibre.

5.1.2 Extracellular matrix

The constitutive description of the ECM in terms of the energy $\mathscr{W}^{\mathrm{M}}$ contains the two material parameters μ^{M} and $\mu_{\mathfrak{cf}}$, which account for the stiffness of the ECM groundmatrix and the collagen type I fibres, respectively.

As explained in Section 3, the groundmatrix energy part $\mathscr{W}^{\mathrm{M}}_{\mathrm{g}}$ and its material parameter μ^{M} account for the non-collageneous parts of the extracellular matrix, which are, for instance, the elastin fibres and proteoglycans. Reported values for the Neo-Hookean stiffness parameter μ^{M} are given by Holzapfel and Weizsäcker [1998] as $61.046\,\mathrm{kN/m^2}$ for the rat abdominal aorta and as $9.5852\,\mathrm{kN/m^2}$ for the rat tail artery. The extensive study of Holzapfel et al. [2005] on human coronary arteries reported $15.12\,\mathrm{kN/m^2} \pm 9.32\,\mathrm{kN/m^2}$ for the adventia, $2.54\,\mathrm{kN/m^2} \pm 1.26\,\mathrm{kN/m^2}$ for the media and $55.8\,\mathrm{kN/m^2} \pm 21.18\,\mathrm{kN/m^2}$ for the intima layer. Obviously, the summarised stiffness values show a very broad variation not only between the different types of specimen but also between different subjects of the same tissue type, observable from the the standard deviations in the experiments of Holzapfel et al. [2005]. In general, these variations make it very difficult to find an appropriate and reliable parameter for the ECM groundmatrix, especially for materials where the ECM occupies large portions of the tissue, like in the specimen used in the reported experiments. In muscle tissue, however, the groundmatrix of extracellular matrix content is small and the contribution of the collagen fibres dominate the passive mechanical behaviour of the tissue. Given the range of reported numbers, e. g., Holzapfel et al. [2005], the groundmatrix stiffness parameter is chosen herein as $\mu^{\mathrm{M}} = 40\,\mathrm{kN/m^2}$, which is a reasonable choice given the overall range of reported parameters.

The second material parameter related to the ECM is the stiffness $\mu_{\mathfrak{cf}}$ of a collagen type I fibre. Due to its importance for the mechanical behaviour of many different biological tissues, there exist a comprehensive body of literature about the properties of type I collagen fibres. The general stretch-stress relation of collagen fibres can be described by a flat toe region at the beginning that eventually evolves to a nearly-linear stretch-stress curve after the initially crinkled fibres have been uncurled at higher stretches. Thus, most studies report on the constant stiffness of the linear stretch-strain region in the form of a scalar modulus, which is sometimes also referred to as Young's modulus. However, Young's modulus is no suitable term for a stiffness quantity in the finite deformation regime and the scalar modulus (or an incremental Young's modulus) has to be properly defined. For instance, a scalar nominal tangent moduli can be formulated as $E_{\mathrm{P}} = \partial_\lambda P = \partial^2_{\lambda^2}\mathscr{W}$ and, analogously, a scalar Cauchy tangent moduli might be introduced as $E_{\mathrm{T}} = \lambda\,\partial_\lambda T$, see, Mihai and Goriely [2017]. Therein, $P = \partial_\lambda \mathscr{W}$ denotes a scalar nominal stress, $T = \lambda\,\partial_\lambda \mathscr{W}$ is a scalar Cauchy stress, and λ is the stretch parameter. With these considerations and the definition given in Eq. (28), the parameter $\mu_{\mathfrak{cf}}$ is identified as a constant nominal tangent modulus. From experimental studies, however, the nature of the moduli provided in these studies is not always clear and care needs to be taken. Moreover, experiments based on methods like indentation do not necessarily provide information on the required tensile stiffness due to the anisotropy of the collagen fibres [Wenger et al., 2007]. Further, the experimentally observed collagen stiffness seems to be dependent on the surrounding conditions (e. g., ambient or in solution), see van der Rijt et al. [2006].

Nominal moduli for the tensile stiffness of collagen type I fibrils/fibres were reported by, e. g., Sasaki and Odajima [1996] and Gentleman et al. [2003]. Sasaki and Odajima [1996] reports a value of $43\,\mathrm{GN/m^2}$ and Gentleman et al. [2003] fibre-diameter-dependent values ranging between $26.97\,\mathrm{GN/m^2}$ and $48.47\,\mathrm{GN/m^2}$. In both of these studies, the collagen was extracted from the bovine achilles tendon. Shen et al. [2008] measured moduli in a range of $860 \pm 450\,\mathrm{MN/m^2}$ for collagen extracted from the sea cucumber dermis. These magnitudes were also reported in the studies of van der Rijt et al. [2006], which were used by Gindre et al. [2013] in their simulations. A further option of obtaining the stiffness of collagen fibres is through microstructural studies [Grytz and Meschke, 2009] or through multi-scale simulations that incorporate nanoscale effects [Buehler, 2008, Marino and Wriggers, 2017].

	percentage of dry connective tissue w.r.t. to total dry muscle		**percentage of collagen type I w.r.t. to the sum of types I and III**	
muscle	perimysium ($n^{\mathrm{M}}_{\mathrm{peri}}$)	endomysium ($n^{\mathrm{M}}_{\mathrm{endo}}$)	perimysium ($n^{\mathrm{I}}_{\mathrm{peri}}$)	endomysium ($n^{\mathrm{I}}_{\mathrm{endo}}$)
Psoas major	1.4	0.5	56.8	44.8
Longissimus dorsi	1.7	0.3	75.5	46.7
Pectoralis profundis	4.7	0.3	59.3	41.5
Semitendinosus	6.4	0.1	58.3	43.6
Gastrocnemius	7.0	n.d.	63.5	41.4
Sternomandibularis	3.3	0.5	59.5	41.9

Table 2 Experimental data on the microstructural composition of the perimysial- and endomysial layers for six bovine muscles extracted from data published in Light et al. [1985]. (w.r.t.= with respect to, n.d.=not determined)

5.2 Structural parameters

In addition to the material parameters, the proposed model also requires the specification of the five structural parameters associated with its microstructure, i. e., the two volume fractions n^{M} and n^{I}, and the three parameters λ_{w}, θ_{m} and b describing the collageneous network (cf. Table 1). Assuming experimental muscle tissue specimen sizes in the millimetre or centimetre range, the specimen contain representative amounts of muscle fibres and muscle fibre bundles. Thus, to compare model predictions with experimental results, structural parameters for endo- and perimysium need to be taken into account by appropriate adding or averaging [see also Gindre et al., 2013].

The volume fraction n^{M} accounts for the amount of connective tissue and is obtained by the sum of the perimysial content $n^{\mathrm{M}}_{\mathrm{peri}}$ and the endomysial content $n^{\mathrm{M}}_{\mathrm{endo}}$, hence:

$$n^{\mathrm{M}} \;=\; n^{\mathrm{M}}_{\mathrm{peri}} + n^{\mathrm{M}}_{\mathrm{endo}}\,. \tag{43}$$

For bovine muscles, Purslow [2010] reported values in the range of $0.43\% - 4.6\%$ for $n^{\mathrm{M}}_{\mathrm{peri}}$ and $0.47\% - 1.2\%$ for $n^{\mathrm{M}}_{\mathrm{endo}}$. In general, they observed higher variations for the perimysium than for the endomysium. Light et al. [1985] presented an extensive study on six different types of bovine muscles and reported $1.4\% - 7.0\%$ for $n^{\mathrm{M}}_{\mathrm{peri}}$ and $0.1\% - 0.5\%$ for $n^{\mathrm{M}}_{\mathrm{endo}}$. The experimental results of Light et al. [1985] are summarised in Table 2. For the volume fraction n^{M} (without distinguishing between peri- and endomysial contribution), Lieber et al. [2003] found a value of 5%.

The volume fraction n^{I} can be calculated by a weighted mean between the peri- and the endomysial tissues via

$$n^{\mathrm{I}} \;=\; \frac{n^{\mathrm{M}}_{\mathrm{peri}}\, n^{\mathrm{coll}}_{\mathrm{peri}}\, n^{\mathrm{I\&III}}_{\mathrm{peri}}\, n^{\mathrm{I}}_{\mathrm{peri}} + n^{\mathrm{M}}_{\mathrm{endo}}\, n^{\mathrm{coll}}_{\mathrm{endo}}\, n^{\mathrm{I\&III}}_{\mathrm{endo}}\, n^{\mathrm{I}}_{\mathrm{endo}}}{n^{\mathrm{M}}_{\mathrm{peri}} + n^{\mathrm{M}}_{\mathrm{endo}}}\,. \tag{44}$$

Therein, $n^{\mathrm{coll}}_{\mathrm{peri}}$ and $n^{\mathrm{coll}}_{\mathrm{endo}}$ account for the amount of collageneous tissue inside the respective connective tissues, while $n^{\mathrm{I\&III}}_{\mathrm{peri}}$ and $n^{\mathrm{I\&III}}_{\mathrm{endo}}$ describe the amount of collagen type I & III fibres inside the respective collageneous tissues. Based on the works of Light and Champion [1984] and Light et al. [1985], $n^{\mathrm{coll}}_{\mathrm{peri}}$ is 95.3%, $n^{\mathrm{coll}}_{\mathrm{endo}}$ is 42.4%, and $n^{\mathrm{I\&III}}_{\mathrm{peri}}$ is equal to $n^{\mathrm{I\&III}}_{\mathrm{endo}}$ and 95%. Table 2 lists $n^{\mathrm{I}}_{\mathrm{peri}}$ and $n^{\mathrm{I}}_{\mathrm{endo}}$ for six bovine muscles. For the semitendinosus muscle, for example, n^{I} is 0.52 and for psoas major, n^{I} is 0.43. This coincides with the range of values reported in Listrat et al. [1999].

For the waviness parameter λ_{w}, we refer to a recent study of Mohammadkhah et al. [2018]. They comprehensively investigated the waviness of collagen fibres in chicken and porcine skeletal muscle tissue for the undeformed and for various deformed states. Mohammadkhah et al. [2018] experimentally determined for the reference configuration a λ_{w} between 1.12 and 1.17. For completeness, we also refer to the images in the works of Rowe [1974] and Trotter and Purslow [1992], where the crinkled state of the fibres is depicted very nicely and which can serve as a basis for an image-based estimation of the waviness parameter.

The mean orientation θ_{m} of the collagen fibre type I fibres in the perimysial layer is frequentely reported to be around 55 degree, see, e. g., Rowe [1974], Purslow [1989], or Purslow [2010]. In the endomysial layer, θ_{m} is found to be around 59 degree, see, e. g., Purslow and Trotter [1994].

Further, the parameter b describes the spreading/dispersion of the collagen type I fibres around the mean orientation θ_{m}. Figure 4 shows the probability density function $\wp_\theta$ for the relevant range of

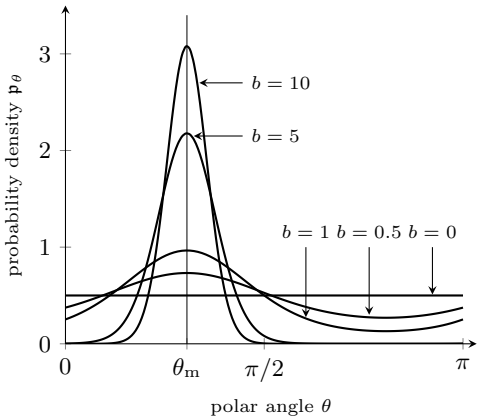

Fig. 4 Plot of the polar probability density function $\mathfrak{p}_\theta$ for different values $\{0, 0.5, 1, 5, 10\}$ of the spreading parameter b around a mean angle θ_m.

b. Comparing these probabilities to experimentally measured distributions for the endomysial layer by Purslow and Trotter [1994], it can be concluded that b ranging between 1 and 10 is a reasonable choice.

For completeness, if distinct values are given for the peri- and the endomysium, the network quantities λ_w, θ_m, b are derived by a weighted averaging

$$\Gamma = \frac{n^M_{peri}\,\Gamma_{peri} + n^M_{endo}\,\Gamma_{endo}}{n^M_{peri} + n^M_{endo}} \tag{45}$$

between the peri- and endomysial quantities, Γ_{peri} and Γ_{endo}, for $\Gamma = \{\lambda_w, \theta_m, b\}$.

6 Results & Discussion

In this section, results for the previously introduced muscle model are presented and discussed. As the focus of this research is on proposing a new microstructurally-based constitutive law for passive skeletal muscle tissue, we focus on the microstructure-originated characteristics of the presented constitutive description rather than on an extensive calibration of the model parameters to macroscopic experiments. Further, the following examples shall depict the capabilities of the new model to predict macroscopic properties without explicitly assuming them in the form of macroscopic constitutive assumptions. In this sense, we first present in Section 6.1 results for the collagen fibre stretch in order to demonstrate that the microstructure exhibits distinct reactions if subjected to different macroscopic deformations.

Moreover, we will show that a few microscopic model parameters are sufficient to capture with the new model the experimentally-observed anisotropic mechanical behaviour of skeletal passive muscle tissue, in paticular if the tissue is subjected to uniaxial tension experiments in muscle fibre direction (Section 6.2) and transverse to the muscle fibre direction (Section 6.3).

The dependence of the new model on the full set of transversely isotropic invariants will be highlighted in Sections 6.4 and 6.5, where it is shown that the $\bar{I}_2$- and $\bar{J}_5$-dependencies are direct consequences of the presented multi-scale modelling framework without the need of calibrating any according macroscopic material parameter.

6.1 Macroscopically-driven collagen fibre stretch

First, we investigate the potential of choosing a comprehensive description for the collagen fibre kinematics as introduced within this model. The deformation of the collagen fibres on the microscale is driven by the macroscopic deformation, $\bar{\boldsymbol{F}}$, and comprises a length change and a reorientation of the collagen fibre end-to-end axis. Thereby, the collagen kinematics follow in the presented model from the

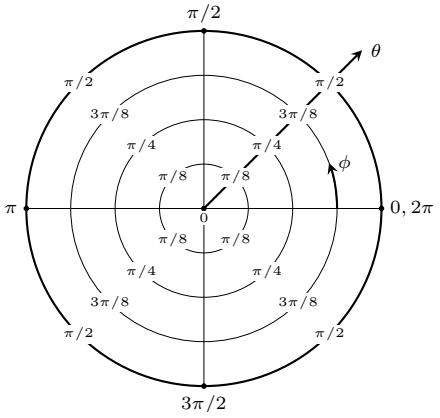

Fig. 5 Illustration of the azimuthal equidistant projection over the upper half of the unit sphere. The azimuthal angle of the three-dimensional space, ϕ, is depicted in the two-dimensional projection as angular/azimuthal angle, while the polar angle θ is depicted in radial direction and ranges from 0 to $\pi/2$.

detailed description of the microstructure and are not artificially introduced as a macroscopic constitutive assumption. This clearly distinguishes the proposed model from other microstructurally-based muscle models like Gindre et al. [2013] and Spyrou et al. [2017, 2019].

For a fibre, which is parametrised by vector $\mathfrak{a}_0$ (cf. Eq. (21)), length changes due to general macroscopic loadings are given by $\lambda_\mathfrak{a}$ (cf. Eq. (38)). First, we investigate the microscopic collagen fibre stretch as a consequence of applying certain specific macroscopic loading conditions. This is achieved by subsequentely simplifing Eq. (38) for the cases of pure uniaxial stretch ($\bar{\gamma}_\mathrm{l} = \bar{\gamma}_\mathrm{t} = 0$), longitudinal shear ($\bar{\lambda}_\mathrm{l} = 1$, $\bar{\gamma}_\mathrm{t} = 0$), and transverse shear ($\bar{\lambda}_\mathrm{l} = 1$, $\bar{\gamma}_\mathrm{l} = 0$). To illustrate the fibre stretch $\lambda_\mathfrak{a}$ over the range of θ and ϕ, we make use of an azimuthal equidistant projection plot. In such plots, the upper half of a three-dimensional unit sphere is projected onto a two-dimensional plane, see Figure 5. The restriction to the upper half sphere ($\theta \in [0, \pi/2]$) is justified by symmetry and a clearer visualisation of the results. Further, since the investigations in this section are purely kinematical, no model parameters have to be specified.

For uniaxial stretch in the preferred direction ($\bar{\gamma}_\mathrm{l} = \bar{\gamma}_\mathrm{t} = 0$), relation (38) for the collagen stretch can be simplified to

$$\lambda_\mathfrak{a}\Big|_{\bar{\gamma}_\mathrm{l}=\bar{\gamma}_\mathrm{t}=0} = \left\{(\bar{\lambda}_\mathrm{l}^3 \cos^2[\theta] + \sin^2[\theta])/\bar{\lambda}_\mathrm{l}\right\}^{1/2}, \tag{46}$$

and the stretch becomes independent of the azimuthal angle ϕ and the coupling invariant $\bar{\psi}_\gamma$. A collagen-stretch model of form (46) was also proposed by Purslow [1989] and serves as full kinematical description for the collagen fibres in, for example, Gindre et al. [2013] and Spyrou et al. [2017, 2019]. However, in those works, relation (46) is constitutively obtained by considering the change in length of the diagonal of a rectangle, where the latter depicts the unwrapped surface of an incompressible cylinder subject to a stretch $\bar{\lambda}_\mathrm{l}$. In contrast, in the proposed model Eq. (46) is directly obtained from the microscopic descriptions of the collageneous structure. This rigorous microstructural approach will especially prove to be beneficial when the collagen fibres are subjected to general and more complex macroscopic deformations.

Figure 6a depicts the resulting projection plot for the collagen stretch $\lambda_\mathfrak{a}$ for a macroscopic stretch of $\bar{\lambda}_\mathrm{l} = 1.675$. The plot exhibits radial symmetry due to the ϕ-independence of relation (46). Moreover, the maximum value for the collagen stretch occurs at $\theta = 0$ and is equal to the applied macroscopic stretch $\bar{\lambda}_\mathrm{l}$, whereas the minimum value at $\theta = \pi/2$ is exactly the transverse stretch $1/\sqrt{\bar{\lambda}_\mathrm{l}}$. The stretch $\bar{\lambda}_\mathrm{l} = 1.675$ is chosen such that the axisymmetric shear, which is defined as $\bar{\gamma}_\mathrm{a} = \pm\{\bar{\lambda}_\mathrm{l}^2 + 2/\bar{\lambda}_\mathrm{l} - 3\}^{1/2}$, is 1.0. Therein, the plus and the minus sign correspond to tension ($\bar{\lambda}_\mathrm{l} > 1$) and to compression ($\bar{\lambda}_\mathrm{l} < 1$), respectively, whereas $\bar{\gamma}_\mathrm{a} = 0$ for $\bar{\lambda}_\mathrm{l} = 1$. Note, without the shear parameter $\bar{\gamma}_\mathrm{a}$, one would not obtain comparability between the axisymmetric shear and the other two shear loadings.

Figure 6b shows the distribution of the collagen fibre stretch for a macroscopic compressive stretch of $\bar{\lambda}_\mathrm{l} = 0.539$, which corresponds to $\bar{\gamma}_\mathrm{a} = -1$. The plot is radial symmetric like Figure 6a. However, the minimum value of the collagen stretch now occurs at $\theta = 0$ and equals the applied macroscopic stretch $\bar{\lambda}_\mathrm{l}$, while the maximum value is observed at $\theta = \pi/2$.

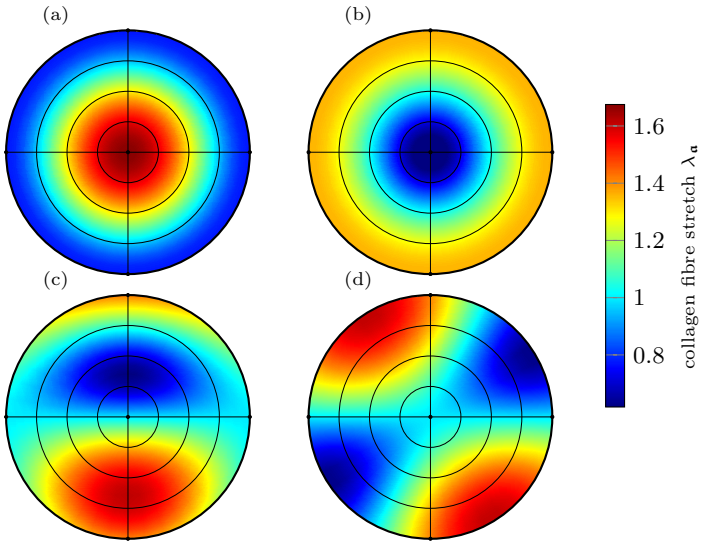

Fig. 6 Projection plot of the collagen fibre stretch $\lambda_{\mathfrak{a}}$ due to (a) a uniaxial tensile stretch $\bar{\lambda}_{\mathrm{l}} = 1.675$ in preferred direction $\bar{\boldsymbol{a}}$, (b) a uniaxial compressive stretch $\bar{\lambda}_{\mathrm{l}} = 0.539$, (c) a longitudinal shear deformation $\bar{\gamma}_{\mathrm{l}} = 1.0$ with $\bar{\psi}_{\gamma} = 0$ and (d) a transversal shear deformation $\bar{\gamma}_{\mathrm{t}} = 1.0$. The range of values is $\lambda_{\mathfrak{a}} \in \{0.773, 1.675\}$ for (a), $\lambda_{\mathfrak{a}} \in \{0.539, 1.362\}$ for (b), and $\lambda_{\mathfrak{a}} \in \{0.618, 1.618\}$ for (c) and (d).

For a longitudinal shear deformation ($\bar{\lambda}_{\mathrm{l}} = 1, \bar{\gamma}_{\mathrm{t}} = 0$), Eq. (38) simplifies to

$$\lambda_{\mathfrak{a}}\Big|_{\bar{\lambda}_{\mathrm{l}}=1,\bar{\gamma}_{\mathrm{t}}=0} = \Big\{ \sin^2[\theta] - \\ - (\bar{\gamma}_{\mathrm{l}} \sin[\theta] \sin[\phi - \bar{\psi}_{\gamma}] - \cos[\theta])^2 \Big\}^{1/2} . \tag{47}$$

In contrast to Eq. (46) of the previously investigated uniaxial loading case, the collagen fibre stretch is now dependent on the azimuthal angle ϕ and the macroscopic coupling invariant $\bar{\psi}_{\gamma}$. However, the dependence on $\bar{\psi}_{\gamma}$ only phase shifts the collagen stretch with respect to the azimuthal orientation and does not alter the averaged results after the integration over the range $\phi \in [0, 2\pi)$ within the operator $\langle(\cdot)\rangle_{\Omega}$. Hence, the network energy $\mathscr{W}_{\mathrm{c}}^{\mathrm{M}}$ is for the longitudinal shear independent on the choice of $\bar{\psi}_{\gamma}$. This confirms the statement that $\bar{\psi}_{\gamma}$ can be chosen arbitrarily whenever $\bar{\gamma}_{\mathrm{l}}\,\bar{\gamma}_{\mathrm{t}} = 0$ (cf., Section 4). The collagen stretches resulting from $\bar{\gamma}_{\mathrm{l}} = 1.0$ and $\bar{\psi}_{\gamma} = 0$ in Eq. (47) are plotted in Figure 6c.

For transversal shear, the collagen stretch is given by

$$\lambda_{\mathfrak{a}}\Big|_{\bar{\lambda}_{\mathrm{l}}=1,\bar{\gamma}_{\mathrm{l}}=0} = \Big\{ \cos^2[\theta] + \\ + \sin^2[\theta] \left(\sin^2[\phi] + (\cos[\phi] - \bar{\gamma}_{\mathrm{t}} \sin[\phi])^2 \right) \Big\}^{1/2} . \tag{48}$$

This relation is independent of the coupling invariant $\bar{\psi}_{\gamma}$ as expected. The result for a transversal shear $\bar{\gamma}_{\mathrm{t}} = 1.0$ is shown in Figure 6d. As for the longitudinal shear, the dependence on the azimuthal angle ϕ indicates that this projection plot does not obey radial symmetry.

In order to highlight the generality of Eq. (38), we also want to investigate the scenario of combined axisymmetric, longitudinal and transversal shear deformation with $\bar{\lambda}_{\mathrm{l}} = 1.675$ (corresponding to $\bar{\gamma}_{\mathrm{a}} = 1.0$) and $\bar{\gamma}_{\mathrm{l}} = \bar{\gamma}_{\mathrm{t}} = 1.0$. Under these conditions, the collagen stretch $\lambda_{\mathfrak{a}}$ additionally depends on the coupling invariant $\bar{\psi}_{\gamma}$. Figure 7 exemplary shows the collagen stretch for four different values, i. e., for $\bar{\psi}_{\gamma} = \{0, 1, 2, 3\}$. From Figure 7, one clearly observes that the four different loadings not only cause a phase shift but also affect the results of the integration when evaluating the averaging operation $\langle(\cdot)\rangle_{\Omega}$ in Eq. (29) and, hence, the network energy $\mathscr{W}_{\mathrm{c}}^{\mathrm{M}}$.

Concluding this section, we want to stress that the comprehensive description for the collagen fibre kinematics within the presented model results in distinct fibre-stretch distributions for different macroscopic deformations. By recalling the case distinction in the collagen fibre energy as defined in Eq. (28), it becomes clear that the detailed knowledge about the stretch distribution is essential

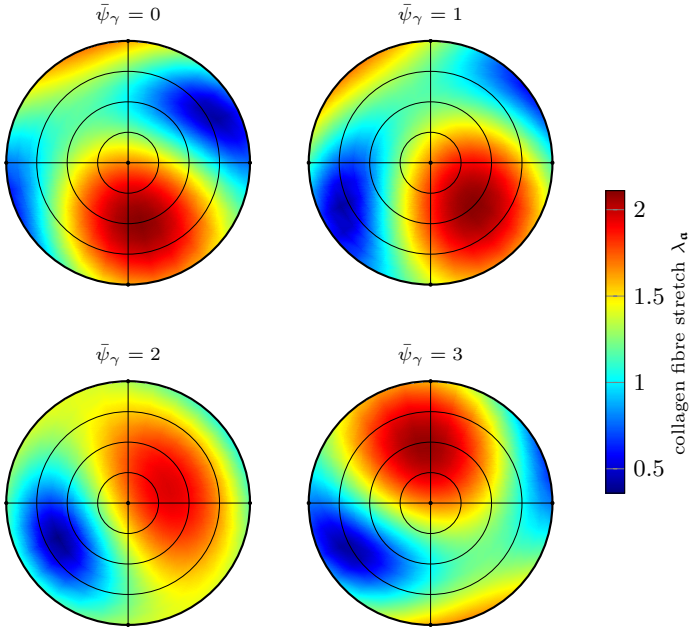

Fig. 7 Projection plot of the collagen fibre stretch $\lambda_{\mathfrak{a}}$ due to a combined stretch and shear loading with $\bar{\lambda}_{\mathrm{l}} = 1.675$, $\bar{\gamma}_{\mathrm{l}} = \bar{\gamma}_{\mathrm{t}} = 1.0$, and four different values $\{0, 1, 2, 3\}$ of the coupling invariant $\bar{\psi}_\gamma$. The range of values over all four cases is $\lambda_{\mathfrak{a}} \in \{0.359, 2.110\}$.

for the exclusion of fibres which are not stretched beyond the waviness threshold, hence for fibres with $\lambda_{\mathfrak{a}} < \lambda_{\mathrm{w}}$, which should not contribute to the network energy. This switch is very important in collageneous tissue [e. g. Holzapfel and Ogden, 2015] and the present model includes the switch for general macroscopic loadings in a natural way without the need of computing critical angles or any other additional procedure.

6.2 Uniaxial tension in muscle fibre direction

Most mechanical tests on skeletal muscle tissue are tension tests in the direction of the muscle fibre orientation, e. g., in Hawkins and Bey [1994], Calvo et al. [2010], Morrow et al. [2010], and Takaza et al. [2013]. Figure 8 shows the results of these experimental studies in one graph. This figure impressively demonstrates the large inter-tissue variations, since Hawkins and Bey [1994] and Calvo et al. [2010] performed experiments on the rat tibialis anterior, Morrow et al. [2010] on the rabbit digitorum longus muscle, and Takaza et al. [2013] on the pig longissimus dorsi muscle. Noticable are the different shapes of the stress-strain relations, which strongly indicates microstructural alterations in the specimen. In addition, Figure 8 shows the large intra-tissue variations, visible through the large standard deviation in the experiments of Calvo et al. [2010]. This suggests that microstructural variations are also present among specimen of the same muscle type.

In what follows, we demonstrate the proposed model's ability to capture such variations by varying the model parameters for ranges reported in literature and summarised in Section 5. Note, we do not aim to calibrate the model to macroscopic experimental data. The macroscopic behaviour should be a consequence of microstructurally changes and not the microstructural material parameters a consequence of macroscopic behaviour, i. e., we aim for a biophysical material description rather than a macroscopic phenomenological description. A description based on macroscopic calibration does not make sense within the context of this work, as we aim to investigate how changes in the microstructural components effect the macroscopic behaviour.

To demonstrate the model's ability to capture microstructural variations on the macroscopic scale, we assume $n^{\mathrm{M}} \in \{0.02, 0.065\}$ and $n^{\mathrm{I}} \in \{0.63, 0.52\}$ (i. e., the values for the longissimus dorsi and semitendinosus given in Table 2). The values for the collagen stiffness are $\mu_{\mathfrak{cf}} = \{300, 500\}$ MN/m^2 and four distinct waviness parameters, i. e., $\lambda_{\mathrm{w}} \in \{1.05, 1.1, 1.15, 1.2\}$. The remaining parameters are

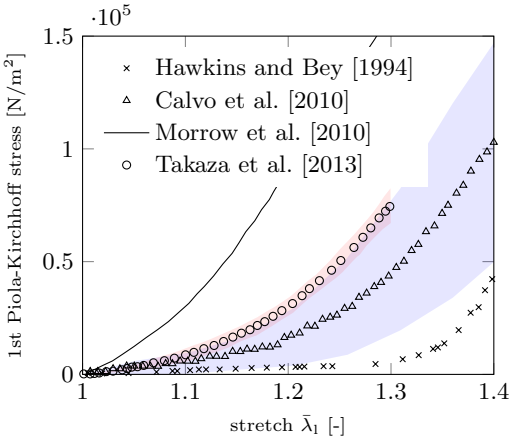

Fig. 8 Collection of tensile experiments on skeletal muscle tissue. The blue and red shaded areas depict the standard deviations of the results of Calvo et al. [2010] and Takaza et al. [2013], respectively. The experiments of Hawkins and Bey [1994] and Calvo et al. [2010] were performed on rat tibialis anterior muscles, whereas Morrow et al. [2010] used rabbit digitorum longus muscles and Takaza et al. [2013] used pig longissimus dorsi muscles.

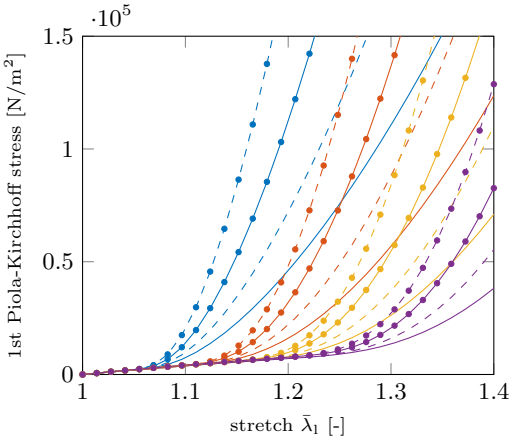

Fig. 9 Collection of simulation results for uniaxial tension and different combinations of model parameters. Lines without and with markers depict volume fractions according to longissimus dorsi and semitendinosus, respectively. Solid and dashed lines define the different collagen stiffnesses $\mu_{\mathfrak{cf}} = \{300, 500\}$ MN/m^2, and the line colors {blue, red, yellow, purple} stand for the different wavinesses $\lambda_\mathrm{w} = \{1.05, 1.1, 1.15, 1.2\}$. The plot range is chosen according to Figure 8.

$\mu^\mathrm{F} = 13.446\,\mathrm{kN/m^2}$, $\mu^\mathrm{M} = 40\,\mathrm{kN/m^2}$, $\theta_\mathrm{m} = 55°$, and $b = 5$. The amount of parameter combinations was chosen such that individual stretch-stress curves can still be distinguished and linked to the according parameters. Further, the deformation gradient is given by $\bar{\boldsymbol{F}} = \bar{\lambda}_\mathrm{l}^{-1/2}(\boldsymbol{e}_1 \otimes \boldsymbol{e}_1 + \boldsymbol{e}_2 \otimes \boldsymbol{e}_2) + \bar{\lambda}_\mathrm{l}\,\boldsymbol{e}_3 \otimes \boldsymbol{e}_3$ and $\bar{\boldsymbol{a}} = \boldsymbol{e}_3$. The stress responses for $\bar{\lambda}_\mathrm{l} \in [1.0, 1.4]$ are shown in Figure 9. By comparing Figure 8 with Figure 9, one observes that the range of simulation results qualitatively matches the experimentally measured stress curves. Individual characteristics and shapes of the experimental curves, for example shorter or longer toe region, can be represented by the model by altering the respective microstructural parameters, for example the waviness λ_w. The exact correlation of the model parameters on specific regions of the stretch-stress-curve would require an appropriate sensitivity analysis on the parameters, which is not the scope of this paper. However, a schematic diagram for the main influence regions of the model parameters during uniaxial stretch can be provided in form of Figure 10, where it is especially highlighted that the amount and the stiffness of collagen type I fibres influence the slope of the curve at higher stretches.

A quantitative comparison between experimental results and our proposed approach does not make sense, since none of the existing experimental studies report on the required microstructural compo-

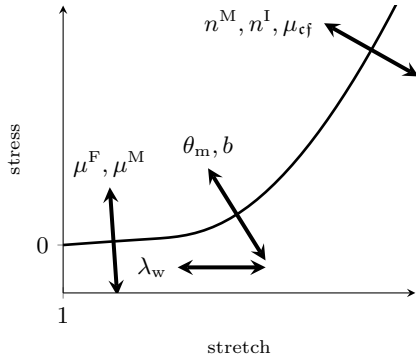

Fig. 10 Schematic diagram of the main influence regions of the model parameters on the strain-stress-curve of skeletal muscle tissue subject to uniaxial tension in muscle fibre direction.

nents are needed for our proposed approach. Moreover, the workflow from cutting, freezing, thawing to testing of tissue specimen encompasses many challenges and even small changes within the prepared tissue may alter the experimental results. Hence only a qualitative comparison is possible. On the other hand, one can systematically alter material parameters and hence systematiclly investigate how the variation of individual components alter the macroscopic behaviour using well-defined in-silico experiments.

A further long-known issue in modelling soft biological tissue is the identification of the stress-free reference configuration. This is a particular challenge for materials with a prominent toe region at low stretches. This uncertainty in defining the stress-free reference configuration can cause large shifts in the stretch-strain curves and differences between simulations and experiments.

Further, we want to remark that for uniaxial deformations the affinity assumption, cf. Eq. (10), depicts an exact result for the considered classes of materials, see, e. g., He et al. [2006] or Agoras et al. [2009]. The collagen fibre kinematics under this loading condition are according to Eq. (46).

6.3 Uniaxial tension transverse to the muscle fibre direction

Next, uniaxial tensile deformation transverse to the muscle fibre direction is considered. To do so, we assume that $\bar{\boldsymbol{a}} = \boldsymbol{e}_3$ and that a stretch λ_1 is applied in $\boldsymbol{e}_1$-direction. Then, with the deformation gradient $\bar{\boldsymbol{F}} = \lambda_1\, \boldsymbol{e}_1 \otimes \boldsymbol{e}_1 + \lambda_2\, \boldsymbol{e}_2 \otimes \boldsymbol{e}_2 + \lambda_3\, \boldsymbol{e}_3 \otimes \boldsymbol{e}_3$, the incompressibility constraint (12) resulting in $\lambda_2 = (\lambda_1 \lambda_3)^{-1}$, and the boundary conditions $\bar{P}_{22} = \bar{P}_{33} = 0$ for the stress tensor coefficients of the unloaded directions, one can compute the remaining unknown stretch λ_3 [Merodio and Ogden, 2005]. Moreover, we choose from the previous section a fixed subset of parameters, which will be used here and in the following examples: $n^{\mathrm{M}} = 0.065$, $n^{\mathrm{I}} = 0.52$, $\mu_{\mathfrak{cf}} = 300 \cdot 10^6\ \mathrm{N/m^2}$, $\lambda_{\mathrm{w}} = 1.1$ and $\mu^{\mathrm{F}} = 13446\,\mathrm{N/m^2}$, $\mu^{\mathrm{M}} = 40 \cdot 10^3\,\mathrm{N/m^2}$, $\theta_{\mathrm{m}} = 55°$, and $b = 5$.

Figure 11 depicts the stress response $\bar{P}_{\mathrm{xf}}$ in $\boldsymbol{e}_1$-direction due to the stretch λ_1. For comparison, the plot also contains the stress response $\bar{P}_{\mathrm{f}}$ if a uniaxial extension $\bar{\lambda}_{\mathrm{l}}$ is applied in muscle fibre direction. The results reveal that the tissue is much stiffer in its transverse direction than in fibre direction. This effect was also experimentally observed by, e. g., Nie et al. [2011], Takaza et al. [2013] or Mohammadkhah et al. [2016]. These matching findings in simulation and experiments also strongly suggests that muscle tissue should not be modelled as a fibre-reinforced material on the macroscopic scale, since the muscle fibres do not necessarily reinforce the material but just lead to an overall transversely isotropic structure.

Further, the differences between the stretches λ_2 and λ_3 in the unloaded directions can be described in terms of Hencky-type Poisson's ratios $\nu^{\mathrm{H}}_{i1} = -\ln[\lambda_i]/\ln[\lambda_1]$ for $i = 2, 3$. Therein, ν^{H}_{i1} depict the extensions of the classical linear Poisson's ratio to the finite-deformation regime based on the logarithmic Hencky strain [Mihai and Goriely, 2017]. The results for ν^{H}_{21} and ν^{H}_{31} are shown in Figure 12. While the mechanical behaviour exhibts isotropic behaviour for low stretches, i. e., $\nu^{\mathrm{H}}_{21} = \nu^{\mathrm{H}}_{31} = 0.5$ for small λ_1-stretches, an anisotropic material behaviour can be observed at higher stretches. In this case, the ratio ν^{H}_{31}, which is related to the muscle fibre direction, significantly increases if compared to ν^{H}_{21},

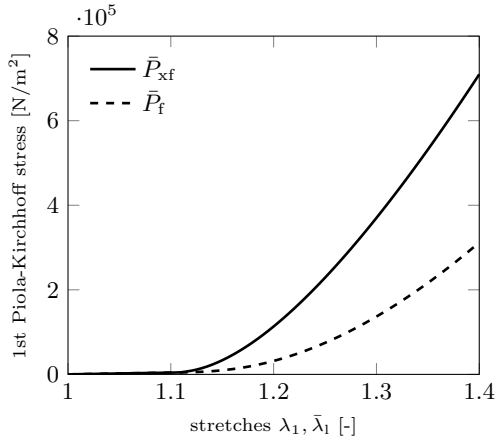

Fig. 11 Stress responses $\bar{P}_{\mathrm{xf}}$ and $\bar{P}_{\mathrm{f}}$ due to a uniaxial stretch λ_1 transverse to the muscle fibre direction or a uniaxial stretch $\bar{\lambda}_{\mathrm{l}}$ in muscle fibre direction, respectively.

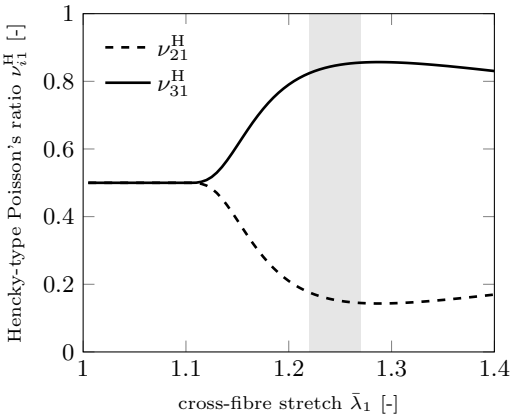

Fig. 12 Hencky-type Poisson's ratios ν^{H}_{21} and ν^{H}_{31} due to the stretch λ_1 transverse to the muscle fibre direction. The shaded area indicates the stretch range in which Takaza et al. [2013] measured nearly constant values for ν^{H}_{21} and ν^{H}_{31}.

which is related to the plane that is transverse to the muscle fibre direction. Note, due to the tissue incompressibility, $\nu^{\mathrm{H}}_{21} + \nu^{\mathrm{H}}_{31} = 1$.

For the considered deformation scenario, Takaza et al. [2013] experimentally measured $\nu^{\mathrm{H}}_{21} = 0.28$ and $\nu^{\mathrm{H}}_{31} = 0.74$. Mohammadkhah et al. [2016] reported $\nu^{\mathrm{H}}_{21} = 0.17$ and $\nu^{\mathrm{H}}_{31} = 0.83$. In order to compare these constant values with the results obtained from our approach, we first need to specify the stretch range in which the experimental values were observed. Takaza et al. [2013] as well as Mohammadkhah et al. [2016] preloaded the tissue specimen before testing. Taking into account the preloading, the range at which Takaza et al. [2013] observed a nearly constant Poisson's ratio is shaded grey in Figure 12, i. e., for $1.22 \leq \lambda_1 \leq 1.27$. In Figure 12, one can see that the simulation also predicts quite constant Poisson ratios with $\nu^{\mathrm{H}}_{21} \in [0.14, 0.18]$ and $\nu^{\mathrm{H}}_{31} \in [0.82, 0.86]$. Further, simulations for this stretch range also agree very well with the experimental results of Mohammadkhah et al. [2016].

6.4 Simple shear deformation

For a transversely isotropic material with preferred direction $\bar{\boldsymbol{a}} = \boldsymbol{e}_3$, one can distinguish between a longitudinal (out-of-plane) simple shear $\bar{\boldsymbol{F}} = \boldsymbol{I} + \bar{\gamma}_{\mathrm{l}}\, \boldsymbol{e}_3 \otimes \boldsymbol{e}_1$ and a transversal (in-plane) simple shear $\bar{\boldsymbol{F}} = \boldsymbol{I} + \bar{\gamma}_{\mathrm{t}}\, \boldsymbol{e}_2 \otimes \boldsymbol{e}_1$. Further, an axisymmetric shear deformation is considered for comparison and achieved by applying the uniaxial tension $\bar{\boldsymbol{F}} = \bar{\lambda}_{\mathrm{l}}^{-1/2}(\boldsymbol{e}_1 \otimes \boldsymbol{e}_1 + \boldsymbol{e}_2 \otimes \boldsymbol{e}_2) + \bar{\lambda}_{\mathrm{l}}\, \boldsymbol{e}_3 \otimes \boldsymbol{e}_3$, in which the

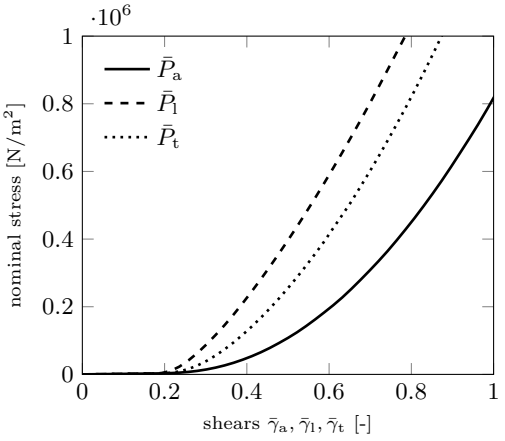

Fig. 13 Comparison of the stresses $\bar{P}_\mathrm{a}$, $\bar{P}_\mathrm{l}$ and $\bar{P}_\mathrm{t}$ resulting from axisymmetric, longitudinal and transversal shear deformations, respectively.

stretch $\bar{\lambda}_\mathrm{l}$ is defined in terms of the axisymmetric shear value $\bar{\gamma}_\mathrm{a}$. Model parameters are chosen as previously (cf. Section 6.3).

Figure 13 shows the results for three shear modes, i. e., for $j = \{\mathrm{a(xisymmetric)}, \mathrm{l(ongitudinal)}, \mathrm{t(ransversal)}\}$ and $\gamma_j \in [0, 1]$. Therein, the results are presented in terms of the nominal stress quantities $\bar{P}_j = \partial_{\gamma_j} \bar{\mathscr{W}}_j$ for $j = \{\mathrm{a}, \mathrm{l}, \mathrm{t}\}$. The stiffest response is observed for the longitudinal shear, while the axisymmetric shear shows the lowest stress response. Note, the collagen fibre stretches, which are due to the three shear modes and which are described by Eqs (46), (47), (48), are visualised in Figures 6a, 6c, 6d, respectively. It has to be pointed out that the distinct stress responses of the three different shear modes are direct consequences of the detailed kinematical description of the collagen fibres described in Eq. (38). In contrast, a model that models collagen solely based on the muscle fibre stretch, $\bar{\lambda}_\mathrm{l}$, as, for example, used by Gindre et al. [2013] or Spyrou et al. [2017], neglects any collagen contribution during longitudinal and/or transversal shear (due to $\bar{\lambda}_\mathrm{l} = 1$). Moreover, being able to capture different mechanical responses for longitudinal ($\bar{\gamma}_\mathrm{l}$) and transversal shear ($\bar{\gamma}_\mathrm{t}$), together with the previous reported link between invariant sets $\mathcal{S}_1$ and $\mathcal{S}_2$ (cf. Eqs (36) and (41)), allows one to conclude a clear dependency of the new model on the macroscopic $\bar{J}_5$-invariant. As a consequence, the proposed macroscopic model naturally depends on invariants $\bar{J}_4$ and $\bar{J}_5$ and not, like for most macroscopically-based muscle models, only on the $\bar{J}_4$-invariant. It is also worth mentioning that the advantage of the presented model is not only that it includes a $\bar{J}_5$-dependence, but that the multi-scale framework and the microstructural parameters completely define how this dependency appears on the macroscale. In contrast, Blemker et al. [2005] considered a $\bar{J}_5$-dependence and thus different longitudinal and transversal shear stiffnesses in their phenomenological model, but set them equal at last because of the lack of macroscopic experimental data to which the model should have been calibrated.

6.5 Coupled shear deformation

Similarly to the investigation of the $\bar{J}_5$-dependence in the previous section, we now investigate the influence of the $\bar{I}_2$-invariant on the overall energy of the new model. With Eqs $(36)_5$ and $(41)_2$ in mind, this dependency is examined by considering coupled shear deformations and varying the coupling invariant $\bar{\psi}_\gamma$. The influence of $\bar{\psi}_\gamma$ on the collagen fibre stretch $\lambda_{\mathfrak{a}}$ has been shown in Section 6.1 and Figure 7. Now, to investigate the influence of the coupling invariant $\bar{\psi}_\gamma$ on the overall energy $\bar{\mathscr{W}}$, the following four different deformations will be considered herein: Coupled longitudinal and transversal shear, i. e., (i) $\bar{\gamma}_\mathrm{l} = \bar{\gamma}_\mathrm{t} = 0.5$, (ii) $\bar{\gamma}_\mathrm{l} = \bar{\gamma}_\mathrm{t} = 1.0$, and the coupling of all three shear modes, i. e., (iii) $\bar{\gamma}_\mathrm{a} = \bar{\gamma}_\mathrm{l} = \bar{\gamma}_\mathrm{t} = 0.5$, and (iv) $\bar{\gamma}_\mathrm{a} = \bar{\gamma}_\mathrm{l} = \bar{\gamma}_\mathrm{t} = 1.0$. Model parameters are chosen as previously (cf. Section 6.3). The results for the macroscopic strain energy $\bar{\mathscr{W}}(\bar{\psi}_\gamma)$ normalised to $\bar{\mathscr{W}}|_{\bar{\psi}_\gamma = 0}$ are shown in Figure 14. The results reveal a pronounced dependency on the coupling invariant $\bar{\psi}_\gamma$, however, the magnitude shows to be dependent on the applied deformation. From the strong $\bar{\psi}_\gamma$-dependency, it follows that the new model exhibits strong emphasis on the macroscopic $\bar{I}_2$-invariant. We want to

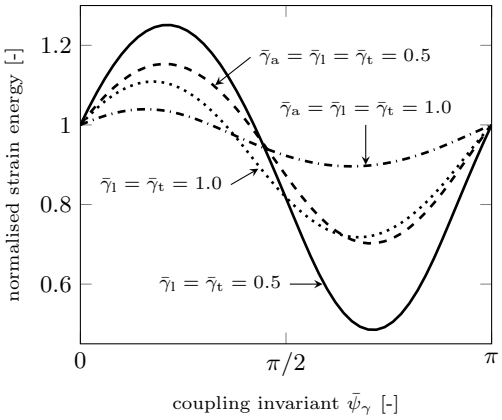

Fig. 14 Normalised strain energies $\bar{\mathscr{W}}/\bar{\mathscr{W}}|_{\bar{\psi}_\gamma=0}$ for four different combinations of coupled shear deformations.

stress again that this dependency is also a direct consequence of the microstructural settings and the choice of the biophysically-motivated model parameters and does not require any calibration on the macroscale.

7 Conclusion

In his work, we introduced a novel multi-scale modelling approach within a continuum-mechanical framework describing the mechanical properties of passive skeletal muscle tissue. The resulting macroscopic model description is entirely based on microstructural components, i. e., the muscle fibres and the extracellular matrix. Further, by introducing volume fractions and following an analytical-homogenisation-based scale transition, an overall constitutive muscle model with eight model parameters is proposed. The key advantage of this approach is that the parameters, which are summarised in Table 1, have *direct microstructural meanings*. Moreover, this novel modelling approach does not require any calibration on the macroscale, on which data obtained from experiments are rather uncertain, limited, simplified, and error-prone. This clearly differentiates the proposed model from all macroscopically-based material models, in which the material parameters are obtained (and limited) through extensive macroscopic calibration to experimental data.

The three material parameters in the new model are directly related to the stiffness of microstructural components and especially the possibility of a direct inclusion of the collagen fibre stiffness proves to be very useful since extensive and reliable data is available in this field. Further, as a consequence of the multi-scale approach, macroscopic material characteristics like incompressibility and transverse isotropy follow *directly from the microscopic considerations* and are not added as constitutive assumptions on the macroscale. In this sense, the presented results focused on emphasising the model capability of predicting macroscopic characteristics directly from the microstructural settings. For instance, it was shown that the transversely isotropic framework relies on all five strain invariants, while for macroscopic-phenomenological muscle models the dependencies have to be included in a constitutive fashion and a lot of models neglect, for example, the $\bar{J}_5$-dependence, hence, shear contributions along the muscle fibre.

The main contribution of this research was to establish a rigorous solid continuum-mechanical basis and to provide an extensible framework for modelling the mechanical behaviour of skeletal muscles. For instance, the present study includes two affinity assumptions, which have to be investigated in follow-up studies. The affinity assumption (10) is inspired by physiological reasons and is expected to be very appropriate. However, this relation may be relaxed by computing the microscopic deformations using well-founded nonlinear homogenisation methods, e. g., the ones proposed by Ponte Castañeda and Tiberio [2000] or Ponte Castañeda [2016]. The second affinity assumption (27) imposes uniformity of the collagen fibres in the extracellular matrix. This topic is subject to a lot of research. A recent study by Krasny et al. [2017], for example, clearly revealed non-affine kinematics of collageneous networks especially at large stretches. However, the moderate differences at physiological stretch ranges for

skeletal muscle also showed a clear justification of the affinity assumption in this study. Nevertheless, non-affine collagen kinematics can be investigated in future studies by incorporating methods on non-uniform fibre networks by, for example, Miehe et al. [2004] or Chen et al. [2011]. Future studies should also further investigate the mechanical structure of the muscle fibre and its resulting influence on the overall muscle behaviour. The experiments of Meyer and Lieber [2011] and Smith et al. [2011] set a solid foundation for assuming a nearly-linear behaviour of the muscle fibre in this work. However, possible anisotropy and more distinct non-linearity of the muscle fibre, as observed by, e. g., Linke et al. [1998], should be investigated. Moreover, the muscle fibre is responsible for the active behaviour of muscle tissue and future extensions of the model thus should include the incorporation of active contractile effects [Paetsch et al., 2012, Röhrle et al., 2008] and according implications on the passive stiffness, like force enhancement [Heidlauf et al., 2016, Herzog, 2018]. It is also possible to extend the description of the muscle fibre and include the activation dynamics by means of a fully coupled chemo-electro-mechanical setup [Heidlauf and Röhrle, 2013].

The new modelling framework offers great potential for a variety of applications, in particular for scenarios where the microstructure of the muscle tissue undergoes morphological changes which can be directly included in the model through the direct adaption of the appropriate biophysically-based model parameters. Such applications where the tissue is subject to significant structural changes are, e. g., immobilisation [Hibino et al., 2008], cerebral palsy [Smith et al., 2011], or botulinum neurotoxin therapies in patients with spasticity [Thacker et al., 2012].

Moreover, the strictly invariant-based formulation of the presented model allows for a straightforward implementation into standard finite-element codes and numerical tools.

Acknowledgements

The research received funding through the Cluster of Excellence for Simulation Technology (ExC 310/2 and ExC 2075) and the European Research Council under the European Unions Seventh Framework Programme (FP/20072013)/ERC Grant Agreement No. 306757 (LEAD). The work of P.P.C. was supported in part by a Research Award from the Alexander von Humboldt Foundation at the University of Stuttgart.

A Derivatives and tensor generators for the collagen fibre stretch $\boldsymbol{\lambda_{\mathfrak{a}}}$ and the invariant set $\boldsymbol{\mathcal{S}_2}$

For a fibre stretch $\lambda_{\mathfrak{a}}$, which is dependent on the invariant set $\mathcal{S}_2$ as defined in Eq. (38), the calculation of the stress tensor $\boldsymbol{P}_{\mathrm{c}}^{\mathrm{M}}$ in Eq. (40) includes the terms $\partial_{\mathfrak{I}}\lambda_{\mathfrak{a}}\,\partial_{\bar{\boldsymbol{F}}}\mathfrak{I}$ for $\mathfrak{I}\in\mathcal{S}_2$ due to the chain rule. In practice, it proofs useful to perform the equivalent calculation $\partial_{\mathfrak{I}'}\lambda_{\mathfrak{a}}\,\partial_{\bar{\boldsymbol{F}}}\mathfrak{I}'$ for $\mathfrak{I}'\in\mathcal{S}_2'$ based on a slighty different invariant set $\mathcal{S}_2'=\{\bar{\lambda}_{\mathrm{l}}^2,\bar{\gamma}_{\mathrm{l}}^2,\bar{\gamma}_{\mathrm{t}}^2,\bar{\psi}_\gamma\}$, which leads to nicer expressions of the tensor bases $\partial_{\bar{\boldsymbol{F}}}\mathcal{I}'$ and avoids some possible zero terms in the denominators for vanishing shears. The four scalar derivatives $\partial_{\mathfrak{I}'}\lambda_{\mathfrak{a}}$ are then given by

$$
\begin{aligned}
\partial_{\bar{\lambda}_{\mathrm{l}}^2}\lambda_{\mathfrak{a}} \;=\; & \big\{2\,\bar{\lambda}_{\mathrm{l}}^3\,\cos^2[\theta]\,+\\
& +\,\sin^2[\theta]\,(\sqrt{\bar{\lambda}_{\mathrm{l}}}\,\bar{\gamma}_{\mathrm{t}}\,\sin[\phi]\,\cos[\phi]\;-\;1)\,-\\
& -\,2\,\bar{\lambda}_{\mathrm{l}}^2\,\bar{\gamma}_{\mathrm{l}}\,\sin[\theta]\,\cos[\theta]\,\sin[\phi-\bar{\psi}_\gamma]\big\}/\big\{4\,\bar{\lambda}_{\mathrm{l}}^3\,\lambda_{\mathfrak{a}}\big\}\,,\\
\partial_{\bar{\gamma}_{\mathrm{l}}^2}\lambda_{\mathfrak{a}} \;=\; & \big\{\,\sin[\theta]\,\sin[\phi-\bar{\psi}_\gamma]\,(\bar{\gamma}_{\mathrm{l}}\,\sin[\theta]\,\sin[\phi-\bar{\psi}_\gamma]\,-\\
& -\,\bar{\lambda}_{\mathrm{l}}\,\cos[\theta])\big\}/(2\,\bar{\gamma}_{\mathrm{l}}\,\lambda_{\mathfrak{a}})\,,\\
\partial_{\bar{\gamma}_{\mathrm{t}}^2}\lambda_{\mathfrak{a}} \;=\; & \big\{\,\sin^2[\theta]\,\sin[\phi]\,(\bar{\gamma}_{\mathrm{t}}\,\sin[\phi]\,-\\
& -\,\bar{\lambda}_{\mathrm{l}}^{-1/2}\,\cos[\phi])\big\}/(2\,\bar{\gamma}_{\mathrm{t}}\,\lambda_{\mathfrak{a}})\,,\quad\text{and}\\
\partial_{\bar{\psi}_\gamma}\lambda_{\mathfrak{a}} \;=\; & \big\{\bar{\gamma}_{\mathrm{l}}\,\sin[\theta]\,\cos[\phi-\bar{\psi}_\gamma]\,\cdot\\
& \cdot\,(\bar{\lambda}_{\mathrm{l}}\,\cos[\theta]\;-\;\bar{\gamma}_{\mathrm{l}}\,\sin[\theta]\,\sin[\phi-\bar{\psi}_\gamma])\big\}/\lambda_{\mathfrak{a}}\,.
\end{aligned}
\tag{49}
$$

The four tensor-valued derivatives of the invariants $\mathfrak{I}'$ with respect to a macroscopic deformation gradient $\bar{\boldsymbol{F}}$ are provided by

$$
\begin{aligned}
\partial_{\bar{\boldsymbol{F}}}\bar{\lambda}_{\mathrm{l}}^2 &= 2\,\bar{\boldsymbol{F}}\bar{\boldsymbol{M}}\,,\\
\partial_{\bar{\boldsymbol{F}}}\bar{\gamma}_{\mathrm{l}}^2 &= -\frac{4\,\bar{\lambda}_{\mathrm{l}}^2 + 2\,\bar{\gamma}_{\mathrm{l}}}{\bar{\lambda}_{\mathrm{l}}^2}\,\bar{\boldsymbol{F}}\bar{\boldsymbol{M}} + \\
&\quad + \frac{2}{\bar{\lambda}_{\mathrm{l}}^2}\,(\bar{\boldsymbol{F}}\bar{\boldsymbol{M}}\bar{\boldsymbol{C}} + \bar{\boldsymbol{F}}\bar{\boldsymbol{C}}\bar{\boldsymbol{M}})\,,\\
\partial_{\bar{\boldsymbol{F}}}\bar{\gamma}_{\mathrm{t}}^2 &= 2\,\bar{\boldsymbol{F}} - \frac{2}{\bar{\lambda}_{\mathrm{l}}}\,\bar{\boldsymbol{F}}^{T-1} + \\
&\quad + 2\,\frac{\bar{\lambda}_{\mathrm{l}}^2 + \bar{\lambda}_{\mathrm{l}}^{-1} + \bar{\gamma}_{\mathrm{l}}^2}{\bar{\lambda}_{\mathrm{l}}^2}\,\bar{\boldsymbol{F}}\bar{\boldsymbol{M}} - \\
&\quad - \frac{2}{\bar{\lambda}_{\mathrm{l}}^2}\,(\bar{\boldsymbol{F}}\bar{\boldsymbol{M}}\bar{\boldsymbol{C}} + \bar{\boldsymbol{F}}\bar{\boldsymbol{C}}\bar{\boldsymbol{M}})\,, \quad \text{and}\\
\partial_{\bar{\boldsymbol{F}}}\bar{\psi}_{\gamma} &= \partial_{\bar{I}_2}\bar{\psi}_{\gamma}\,\partial_{\bar{\boldsymbol{F}}}\bar{I}_2\\
&= 2\,\frac{\bar{\lambda}_{\mathrm{l}}^2 + 2\,\bar{\lambda}_{\mathrm{l}}^{-1} + \bar{\gamma}_{\mathrm{l}}^2 + \bar{\gamma}_{\mathrm{t}}^2}{B}\,\bar{\boldsymbol{F}} - \frac{2}{B}\,\bar{\boldsymbol{F}}\bar{\boldsymbol{C}}\,,
\end{aligned}
\tag{50}
$$

where $B = \bar{\gamma}_{\mathrm{l}}^2\,\bar{\gamma}_{\mathrm{t}}\,(\bar{\gamma}_{\mathrm{t}}\,\sin[2\bar{\psi}_{\gamma}] - 2\bar{\lambda}_{\mathrm{l}}^{-1/2}\,\cos[2\bar{\psi}_{\gamma}])$ and $\bar{\boldsymbol{M}}$ is a structure tensor accounting for a preferred direction as introduced in the text. For the derivative $\partial_{\bar{\boldsymbol{F}}}\bar{\psi}_{\gamma}$, use was made of the relation $\partial_{\bar{I}_2}\bar{\psi}_{\gamma} = (\partial_{\bar{\psi}_{\gamma}}\bar{I}_2)^{-1}$ and Eq. $(41)_2$. In the scalar derivatives $\partial_{\bar{\gamma}_{\mathrm{l}}^2}\lambda_{\mathfrak{a}}$, $\partial_{\bar{\gamma}_{\mathrm{t}}^2}\lambda_{\mathfrak{a}}$ as well as in the tensorial derivative $\partial_{\bar{\boldsymbol{F}}}\bar{\psi}_{\gamma}$, shear values occur in the denominator, which seems to produce singularities for vanishing shears. However, the singularities in $\partial_{\bar{\gamma}_{\mathrm{l}}^2}\lambda_{\mathfrak{a}}$ and $\partial_{\bar{\gamma}_{\mathrm{t}}^2}\lambda_{\mathfrak{a}}$ rule out after applying the integrations $\langle\cdot\rangle_{\Omega}$. For the invariant $\bar{\psi}_{\gamma}$, limit values can be found for the cases of vanishing shears $\bar{\gamma}_{\mathrm{l}} = 0$ and/or $\bar{\gamma}_{\mathrm{t}} = 0$, see for example Criscione et al. [2001]. In a numerical setting, zero shear values might be replaced by small near-to-zero values, which can serve as an easy and efficient strategy of avoiding the singular values. For completeness, note that the expressions for $\partial_{\bar{\boldsymbol{F}}}\bar{\lambda}_{\mathrm{l}}^2$, $\partial_{\bar{\boldsymbol{F}}}\bar{\gamma}_{\mathrm{l}}^2$, and $\partial_{\bar{\boldsymbol{F}}}\bar{\gamma}_{\mathrm{t}}^2$ were also provided by deBotton et al. [2006].

References

Advani SG, Tucker III CL. The Use of Tensors to Describe and Predict Fiber Orientation in Short Fiber Composites. Journal of Rheology 1987;31:751–84.

Agoras M, Lopez-Pamies O, Ponte Castañeda P. A general hyperelastic model for incompressible fiber-reinforced elastomers. Journal of the Mechanics and Physics of Solids 2009;57:268–86.

Alastrué V, Martínez MA, Doblaré M, Menzel A. Anisotropic micro-sphere-based finite elasticity applied to blood vessel modelling. Journal of the Mechanics and Physics of Solids 2009;57:178–203.

Asgari M, Latifi N, Heris HK, Vali H, Mongeau L. *In vitro* fibrillogenesis of tropocollagen type III in collagen type I affects its relative fibrillar topology and mechanics. Scientific Reports 2017;7:1–10. doi:10.1038/s41598-017-01476-y.

Ateshian GA, Rajan V, Chahine NO, Canal CE, Hung CT. Modeling the Matrix of Articular Cartilage Using a Continuous Fiber Angular Distribution Predicts Many Observed Phenomena. Journal of Biomechanical Engineering 2009;131:061003–. doi:10.1115/1.3118773.

Bleiler C, Ponte Castañeda P, Röhrle O. Towards effective mechanical properties of skeletal muscle tissue via homogenisation. Proceedings in Applied Mathematics and Mechanics 2015a;15:83–4.

Bleiler C, Ponte Castañeda P, Röhrle O. Multiscale modelling of skeletal muscle tissue by incorporating microstructural effects. Proceedings in Applied Mathematics and Mechanics 2016;16:75–6. doi:10.1002/pamm.201610026.

Bleiler C, Wagner A, Stadelmann VA, Windolf M, Köstler H, Boger A, Gueorguiev-Rüegg B, Ehlers W, Röhrle O. Multiphasic modelling of bone-cement injection into vertebral cancellous bone. International Journal for Numerical Methods in Biomedical Engineering 2015b;31(1):37–57. URL: `http://dx.doi.org/10.1002/cnm.2696`. doi:10.1002/cnm.2696.

Blemker SS, Delp SL. Three-dimensional representation of complex muscle architectures and geometries. Annals of Biomedical Engineering 2005;33:661–73.

Blemker SS, Pinsky PM, Delp SL. A 3D model of muscle reveals the causes of nonuniform strains in the biceps brachii. Journal of Biomechanics 2005;38:657–65.

Boehler JP. A Simple Derivation of Representations for Non-Polynomial Constitutive Equations in Some Cases of Anisotropy. Zeitschrift für Angewandte Mathematik und Mechanik 1979;59:157–67.

Böl M. On a phenomenological model for fatigue effects in skeletal muscles. Journal of Theoretical Biology 2010;doi:doi:10.1016/j.jtbi.2010.03.004.

Böl M, Ehret AE, Leichsenring K, Weichert C, Kruse R. On the anisotropy of skeletal muscle tissue under compression. Acta Biomaterialia 2014;10:3225–34.

Buehler MJ. Nanomechanics of collagen fibrils under varying cross-link densities: Atomistic and continuum studies. Journal of the Mechanical Behavior of Biomedical Materials 2008;1:59–67. doi:10.1016/j.jmbbm.2007.04.001.

Calvo B, Ramírez A, Alonso A, Grasa J, Soteras F, Osta R, Muñoz MJ. Passive nonlinear elastic behaviour of skeletal muscle: Experimental results and model formulation. Journal of Biomechanics 2010;43(2):318–25.

Chen H, Liu Y, Zhao X, Lanir Y, Kassab GS. A micromechanics finite-strain constitutive model of fibrous tissue. Journal of the Mechanics and Physics of Solids 2011;59:1823–37.

Criscione JC, Douglas AS, Hunter WC. Physically based strain invariant set for materials exhibiting transversely isotropic behavior. Journal of the Mechanics and Physics of Solids 2001;49:871–97.

deBotton G, Hariton I, Socolsky EA. Neo-Hookean fibre-reinforced composites in finite elasticity. Journal of the Mechanics and Physics of Solids 2006;54:533–59.

Decraemer WF, Maes MA, Vanhuyse VJ. An elastic stress-strain relation for soft biological tissues based on a structural model. Journal of Biomechanics 1980;13:463–8.

Duance VC, Restall DJ, Beard H, Bourne FJ, Bailey AJ. The location of three collagen types in skeletal muscle. FEBS Letters 1977;79:248–52.

Ehlers W, Wagner A. Multi-component modelling of human brain tissue: a contribution to the constitutive and computational description of deformation, flow and diffusion processes with application to the invasive drug-delivery problem. Computer Methods in Biomechanics and Biomedical Engineering 2015;18:861–79. URL: `https://doi.org/10.1080/10255842.2013.853754`. doi:10.1080/10255842.2013.853754.

Ehret AE, Böl M, Itskov M. A continuum constitutive model for the active behaviour of skeletal muscle. Journal of the Mechanics and Physics of Solids 2011;59:625–36.

Ericksen JL, Rivlin RS. Large Elastic Deformations of Homogeneous Anisotropic Materials. Journal of Rational Mechanics and Analysis 1954;3:281–301.

Federico S, Herzog W. Towards an analytical model of soft biological tissues. Journal of Biomechanics 2008;41:3309–13.

Flory PJ. Thermodynamic relations for high elastic materials. Transactions of the Faraday Society 1961;57:829–38.

Fung YC. Biomechanics - Mechanical Properties of Living Tissues. 2nd ed. New York: Springer-Verlag, 2010.

Geers MGD, Kouznetsova VG, Brekelmans WAM. Multi-scale computational homogenization: Trends and challenges. Journal of Computational and Applied Mathematics 2010;234:2175–82.

Gelse K, Pöschl E, Aigner T. Collagens—structure, function, and biosynthesis. Advanced Drug Delivery Reviews 2003;55:1531–46.

Gentleman E, Lay AN, Dickerson DA, Nauman EA, Livesay GA, Dee KC. Mechanical characterization of collagen fibers and scaffolds for tissue engineering. Biomaterials 2003;24:3805–13.

Gindre J, Takaza M, Moerman KM, Simms CK. A structural model of passive skeletal muscle shows two reinforcement processes in resisting deformation. Journal of the Mechanical Behavior of Biomedical Materials 2013;22:84–94.

Grytz R, Meschke G. Constitutive modeling of crimped collagen fibrils in soft tissues. Journal of the Mechanical Behavior of Biomedical Materials 2009;2:522–33.

Hawkins D, Bey M. A Comprehensive Approach for Studying Muscle-Tendon Mechanics. Journal of Biomechanical Engineering 1994;116:51–5.

He QC, Quang HL, Feng ZQ. Exact Results for the Homogenization of Elastic Fiber-Reinforced Solids at Finite Strain. Journal of Elasticity 2006;83:153–77.

Heidlauf T, Klotz T, Rode C, Altan E, Bleiler C, Siebert T, Röhrle O. A multi-scale continuum model of skeletal muscle mechanics predicting force enhancement based on actin-titin interaction. Biomechanics and Modeling in Mechanobiology 2016;15:1423–37.

Heidlauf T, Klotz T, Rode C, Siebert T, Röhrle O. A continuum-mechanical skeletal muscle model including actin-titin interaction predicts stable contractions on the descending limb of the force-length relation. PLoS Computational Biology 2017;13:e1005773. URL: `https://doi.org/10.1371/journal.pcbi.1005773`. doi:10.1371/journal.pcbi.1005773.

Heidlauf T, Röhrle O. Modeling the Chemoelectromechanical Behavior of Skeletal Muscle Using the Parallel Open-Source Software Library OpenCMISS. Computational and Mathematical Methods in Medicine 2013;2013:14 pages.

Helfenstein J, Jabareen M, Mazza E, Govindjee S. On non-physical response in models for fiber-reinforced hyperelastic materials. International Journal of Solids and Structures 2010;47:2056–61.

Herzog W. The multiple roles of titin in muscle contraction and force production. Biophysical Reviews 2018;10:1187–99.

Hibino I, Okita M, Inoue T, Banno Y, Hoso M. Effect of Immobilization on Insoluble Collagen Concentration and Type I and Type III Collagen Isoforms of Rat Soleus Muscle. Journal of the Japanese Physical Therapy Association 2008;11:1–6.

Hill R. Elastic properties of reinforced solids: Some theoretical principles. Journal of the Mechanics and Physics of Solids 1963;11:357–72.

Hill R. On constitutive macro-variables for heterogeneous solids at finite strain. Proceedings of the Royal Society of London Series A, Mathematical and Physical Sciences 1972;326:131–47.

Holzapfel GA, Ogden RW. On the tension-compression switch in soft fibrous solids. European Journal of Mechanics A/Solids 2015;49:561–9.

Holzapfel GA, Sommer G, Gasser CT, Regitnig P. Determination of layer-specific mechanical properties of human coronary arteries with nonatherosclerotic intimal thickening and related constitutive modeling. American Journal of Physiology-Heart and Circulatory Physiology 2005;289:H2048–58.

Holzapfel GA, Weizsäcker HW. Biomechanical behavior of the arterial wall and its numerical characterization. Computers in Biology and Medicine 1998;28:377–92.
Hurschler C, Loitz-Ramage B, Vanderby R. A Structurally Based Stress-Stretch Relationship for Tendon and Ligament. Transactions of the ASME 1997;119:392–9.
Johansson T, Meier P, Blickhan R. A Finite-Element Model for the Mechanical Analysis of Skeletal Muscles. Journal of Theoretical Biology 2000;206:131–49. doi:10.1006/jtbi.2000.2109.
Kovanen V. Intramuscular Extracellular Matrix: Complex Environment of Muscle Cells. Exercise and Sport Sciences Reviews 2002;30:20–5.
Krasny W, Morin C, Magoariec H, Avril S. A comprehensive study of layer-specific morphological changes in the microstructure of carotid arteries under uniaxial load. Acta Biomaterialia 2017;57:342–51.
Lanir Y. A structural theory for the homogeneous biaxial stress-strain relationships in flat collageneous tissues. Journal of Biomechanics 1979;12:423–36.
Lanir Y. Constitutive equations for fibrous connective tissues. Journal of Biomechanics 1983;16:1–12.
Li Y, Lang P, Linke WA. Titin stiffness modifies the force-generating region of muscle sarcomeres. Scientific Reports 2016;6:1–9. URL: https://doi.org/10.1038/srep24492. doi:10.1038/srep24492.
Lieber RL. Skeletal Muscle. Structure, Function and Plasticity. 3rd ed. Lippincott Williams & Wilkins, 2010.
Lieber RL, Runesson E, Einarsson F, Fridén J. Inferior mechanical properties of spastic muscle bundles due to hypertrophic but compromised extracellular matrix material. Muscle & Nerve 2003;28(4):464–71.
Light N, Champion AE. Characterization of muscle epimysium, perimysium and endomysium collagens. Biochemical Journal 1984;219:1017–26.
Light N, Champion AE, Voyle C, Bailey AJ. The Role of Epimysial, Perimysial and Endomysial Collagen in Determining Texture in Six Bovine Muscles. Meat Science 1985;13:137–49.
Linke WA, Ivemeyer M, Mundel P, Stockmeier MR, Kolmerer B. Nature of PEVK-titin elasticity in skeletal muscle. Proceedings of the National Academy of Sciences 1998;95:8052 8057. URL: https://doi.org/10.1073/pnas.95.14.8052. doi:10.1073/pnas.95.14.8052.
Listrat A, Picard B, Geay Y. Age-related changes and location of type I, III, IV, V and VI collagens during development of four foetal skeletal muscles of double-muscled and normal bovine animals. Tissue & Cell 1999;31:17–27. URL: https://doi.org/10.1054/tice.1998.0015. doi:10.1054/tice.1998.0015.
Maceri F, Marino M, Vairo G. A unified multiscale mechanical model for soft collagenous tissues with regular fiber arrangement. Journal of Biomechanics 2010;43:355–63.
MacIntosh BR, Gardiner PF, McComas AJ. Skeletal Muscle. Form and Function. 2nd ed. Human Kinetics, 2006.
Marino M, Wriggers P. Finite strain response of crimped fibers under uniaxial traction: An analytical approach applied to collagen. Journal of the Mechanics and Physics of Solids 2017;98:429–53.
Merodio J, Ogden RW. Mechanical response of fiber-reinforced incompressible non-linearly elastic solids. International Journal of Non-Linear Mechanics 2005;40:213–27.
Meyer GA, Lieber RL. Elucidation of extracellular matrix mechanics from muscle fibers and fiber bundles. Journal of Biomechanics 2011;44:771–3.
Miehe C. Aspects of the fomulation and finite element implementation of large strain isotropic elasticity. International Journal for Numerical Methods in Engineering 1994;37:1981–2004.
Miehe C. Strain-driven homogenization of inelastic microstructures and composites based on an incremental variational formulation. International Journal for Numerical Methods in Engineering 2002;55:1285–322.
Miehe C, Göktepe S, Lulei F. A micro-macro approach to rubber-like materials–Part I: the non-affine microsphere model of rubber elasticity. Journal of the Mechanics and Physics of Solids 2004;52:2617–60.
Mihai LA, Goriely A. How to characterize a nonlinear elastic material? A review on nonlinear constitutive parameters in isotropic finite elasticity. Proceedings of the Royal Society A 2017;473:1–33. URL: http://dx.doi.org/10.1098/rspa.2017.0607. doi:10.1098/rspa.2017.0607.
Mohammadkhah M, Murphy P, Simms CK. The in vitro passive elastic response of chicken pectoralis muscle to applied tensile and compressive deformation. Journal of the Mechanical Behavior of Biomedical Materials 2016;62:468–80.
Mohammadkhah M, Murphy P, Simms CK. Collagen fibril organization in chicken and porcine skeletal muscle perimysium under applied tension and compression. Journal of the Mechanical Behavior of Biomedical Materials 2018;77:734–44. URL: http://dx.doi.org/10.1016/j.jmbbm.2017.08.007. doi:10.1016/j.jmbbm.2017.08.007.
Morrow DA, Haut Donahue TL, Odegard GM, Kaufman KR. Transversely isotropic tensile material properties of skeletal muscle tissue. Journal of the Mechanical Behavior of Biomedical Materials 2010;3:124–9.
Nemat-Nasser S, Hori M. Micromechanics: overall properties of heterogeneous materials. 2nd ed. Amsterdam: Elsevier, 1999.
Nie X, Cheng JI, Chen WW, Weerasooriya T. Dynamic Tensile Response of Porcine Muscle. Journal of Applied Mechanics 2011;78:1–5.
Paetsch C, Trimmer BA, Dorfmann A. A constitutive model for active-passive transition of muscle fibers. International Journal of Non-Linear Mechanics 2012;47:377–87.
Ponte Castañeda P. The effective mechanical properties of nonlinear isotropic composites. Journal of the Mechanics and Physics of Solids 1991;39(1):45–71.
Ponte Castañeda P. Stationary variational estimates for the effective response and field fluctuations in nonlinear composites. Journal of the Mechanics and Physics of Solids 2016;96:660–82.
Ponte Castañeda P, Suquet P. Nonlinear Composites. Advances in Applied Mechanics 1998;34:171–302.
Ponte Castañeda P, Tiberio E. A second-order homogenization method in finite elasticity and applications to black-filled elastomers. Journal of the Mechanics and Physics of Solids 2000;48:1389–411.

Purslow PP. Strain-induced reorientation of an intramuscular connective tissue network: implications for passive muscle elasticity. Journal of Biomechanics 1989;22:21–31.
Purslow PP. Muscle fascia and force transmission. Journal of Bodywork & Movement Therapies 2010;14:411–7.
Purslow PP, Trotter JA. The morphology and mechanical properties of endomysium in series-fibred muscles: variations with muscle length. Journal of Muscle Research & Cell Motility 1994;15:299–308.
Ricken T, Dahmen U, Dirsch O. A biphasic model for sinusoidal liver perfusion remodeling after outflow obstruction. Biomechanics and Modeling in Mechanobiology 2010;9:435–50.
van der Rijt JAJ, van der Werf KO, Bennink ML, Dijkstra PJ, Feijen J. Micromechanical Testing of Individual Collagen Fibrils. Macromolecular Bioscience 2006;6:697–702.
Röhrle O, Davidson JB, Pullan AJ. Bridging scales: A three-dimensional electromechanical finite element model of skeletal muscle. SIAM Journal on Scientific Computing 2008;30(6):2882–904.
Röhrle O, Pullan AJ. Three-dimensional finite element modelling of muscle forces during mastication. Journal of Biomechanics 2007;40:3363–72.
Rowe RWD. Collagen fibre arrangement in intramuscular connective tissue. Changes associated with muscle shortening and their possible relevance to raw meat toughness measurements. Internation Journal for Food Science and Technology 1974;9:501–8.
Sansour C. On the physical assumptions underlying the volumetric-isochoric split and the case of anisotropy. European Journal of Mechanics A/Solids 2008;27:28–39.
Sasaki N, Odajima S. Elongation mechanism of collagen fibrils and force-strain relations of tendon at each level of structural hierarchy. Journal of Biomechanics 1996;29:1131–6.
Schröder J. A numerical two-scale homogenization scheme: the FE^2-method. In: Schröder J, Hackl K, editors. Plasticity and Beyond. Springer; volume 550 of *CISM International Centre for Mechanical Sciences*; 2014. p. 1–64.
Schröder J, Neff P. Invariant formulation of hyperelastic transverse isotropy based on polyconvex free energy functions. International Journal of Solids and Structures 2003;40:401–45.
Sharifimajd B, Stålhand J. A continuum model for skeletal muscle contraction at homogeneous finite deformations. Biomechanics and Modeling in Mechanobiology 2013;12:965–73.
Shen ZL, Dodge MR, Kahn H, Ballarini R, Eppel SJ. Stress-Strain Experiments on Individual Collagen Fibrils. Biophysical Journal 2008;95:3956–63. doi:10.1529/biophysj.107.124602.
Smith LR, Lee KS, Ward SR, Chambers HG, Lieber RL. Hamstring contractures in children with spastic cerebral palsy result from a stiffer extracellular matrix and increased *in vivo* sarcomere length. Journal of Physiology 2011;589:2625–39.
Spencer AJM. Theory of Invariants. In: Eringen AC, editor. Continuum Physics, Volume 1. New York: Academic Press; 1971. p. 239–353.
Spyrou LA, Agoras M, Danas K. A homogenization model of the voigt type for skeletal muscle. Journal of Theoretical Biology 2017;414:50–61. URL: `http://dx.doi.org/10.1016/j.jtbi.2016.11.018`. doi:10.1016/j.jtbi.2016.11.018.
Spyrou LA, Brisard S, Danas K. Multiscale modeling of skeletal muscle tissues based on analytical and numerical homogenization. Journal of the Mechanical Behavior of Biomedical Materials 2019;92:97–117.
Takaza M, Moerman KM, Gindre J, Lyons G, Simms CK. The anisotropic mechanical behaviour of passive skeletal muscle tissue subjected to large tensile strain. Journal of the Mechanical Behavior of Biomedical Materials 2013;17:209–20.
Talbot DRS, Willis JR. Variational Principles for Inhomogeneous Non-linear Media. IMA Journal of Applied Mathematics 1985;35:39–54.
Thacker BE, Tomiya A, Hulst JB, Suzuki KP, Bremner SN, Gastwirt RF, Greaser ML, Lieber RL, Ward SR. Passive Mechanical Properties and Related Proteins Change with Botulinum Neurotoxin A Injection of Normal Skeletal Muscle. Journal of Orthopaedic Research 2012;30:497–502.
Treloar LRG, Riding G. A non-Gaussian theory for rubber in biaxial strain. I. Mechanical properties. Proceedings of the Royal Society A 1979;369:261–80.
Trotter JA, Purslow PP. Functional Morphology of the Endomysium in Series Fibered Muscles. Journal of Morphology 1992;212:109–22.
Virgilio KM, Martin KS, Peirce SM, Blemker SS. Multiscale models of skeletal muscle reveal the complex effects of muscular dystrophy on tissue mechanics and damage susceptibility. Interface Focus 2015;5:20140080. URL: `http://dx.doi.org/10.1098/rsfs.2014.0080`. doi:10.1098/rsfs.2014.0080.
Voigt W. Theoretische Studien über die Elasticitätsverhältnisse der Krystalle. Abhandlungen der Königlichen Gesellschaft der Wissenschaften in Göttingen 1887;34:3–100.
Wenger MPE, Bozec L, Horton MA, Mesquida P. Mechanical properties of collagen fibrils. Biophysical Journal 2007;93:1255–63.
Zohdi TI, Wriggers P. An Introduction to Computational Micromechanics. 2nd ed. Berlin Heidelberg: Springer-Verlag, 2008.